Aperiodic crystals in biology

JPCM-2021

Aperiodic crystals in biology

Enrique Maciá

Dpto. Física de Materiales, Facultad CC. Fisicas,

Universidad Complutense de Madrid, E-28040, Spain

(Date textdate; Received textdate; Revised textdate; Accepted textdate; Published textdate)

Abstract

Biological systems display a broad palette of hierarchically ordered designs spanning over many orders of magnitude in size. Remarkably enough, periodic order, which profusely shows up in non-living ordered compounds, plays a quite subsidiary role in most biological structures, which can be appropriately described in terms of the more general aperiodic crystal notion instead. In this Topical Review I shall illustrate this issue by considering several representative examples, including botanical phyllotaxis, the geometry of cell patterns in tissues, the morphology of sea urchins, or the symmetry principles underlying virus architectures. In doing so, we will realize that albeit the currently adopted quasicrystal notion is not general enough to properly account for the rich structural features one usually finds in biological arrangements of matter, several mathematical tools and fundamental notions belonging to the aperiodic crystals science toolkit can provide a useful modeling framework to this end.

Contents

I. HIERARCHICALLY ORDERED DESIGNS

Biological structures span over about eleven orders of magnitude in size, ranging from the molecular nanometer-scale, up to the decameter scale displayed by whales in the animal kingdom, and the hectometer range recorded for taller trees in the plant kingdom [1]. If one closely inspects these biological systems at different magnifications, she/he readily realizes that they exhibit hierarchies of structure upon structure all the way through the molecular to the macroscopic domains. Indeed, structural hierarchization appears as a fundamental design principle in biology [2, 3]. Well-known, simple examples of hierarchical structures are provided by fractals, which can be obtained by iteration of a simple rule, whereby at each scale the structure is built from subunits that are replicas of the pattern belonging to the earlier stages [4, 5]. A suitable example of a fractal structure, exhibiting a characteristic scale-invariance symmetry with a scale factor $\lambda = 1 + 2\sqrt{3}/3$ is shown in Fig.1A. Various

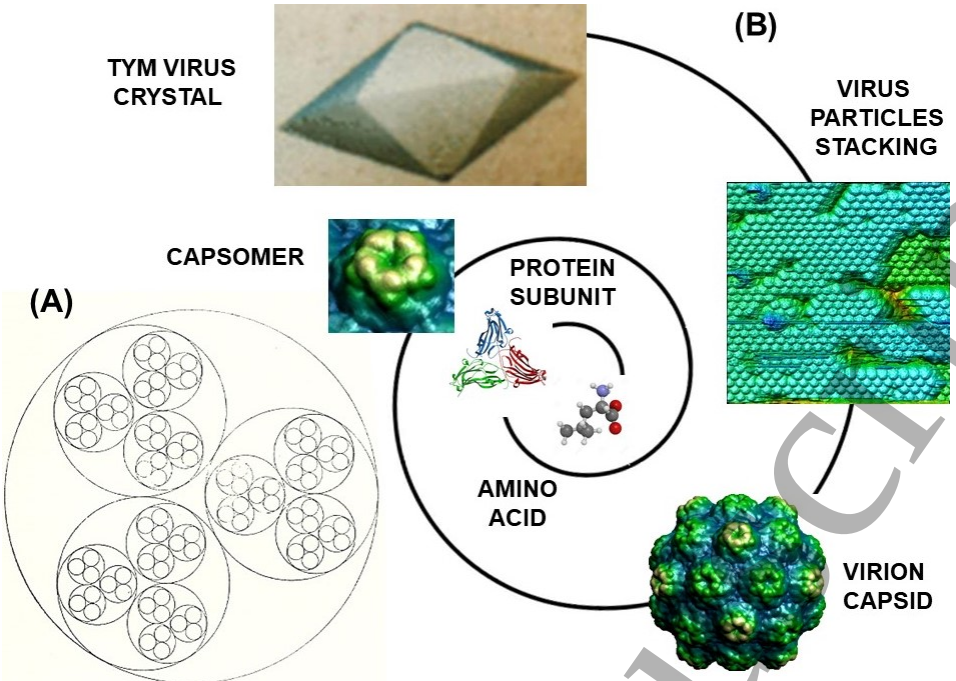

FIG. 1: (A) Five orders of a sequence of nested inscribed circles. Each structural stage contains three units of the preceding one. (B) Nested stages in a turnip yellow mosaic (TYM) virus crystal structure [6] (Creative Commons Attribution 4.0 International License). This organic supramolecular crystal is composed of polyhedral virus particles, whose shell is made of protein subunits grouped in ordered capsomers (adapted from [7, 8]). In turn, these proteins are made of amino acid building blocks. Inside the capsid we have a nucleic acid macromolecule (DNA or RNA) which is composed of nucleotides (not shown for the sake of simplicity). The frames are successively plotted along an expanding spiral curve in order to highlight the important role played by a hierarchical succession of scale transformations in the virus crystal overall design.

biological structures have been shown to display fractal-like properties, such as an approximate scale invariance over a restricted spatial scale, and a spatial distribution which can be reasonably measured in terms of suitable fractal dimensions [9]. Nevertheless, ideal mathematical fractals are homogeneous structures exhibiting exact scale-invariance symmetry, whereas in actual biological patterns we observe the emergence of novel structural designs at a given scale which are not present in the scales below and/or above. This important feature is illustrated in Fig.1B, where we see that TYM virus crystals (space group $P6_222$, with unit cell parameters $a = b = 54$ nm, $c = 32$ nm [10]), exhibiting a hexagonal bipyramid

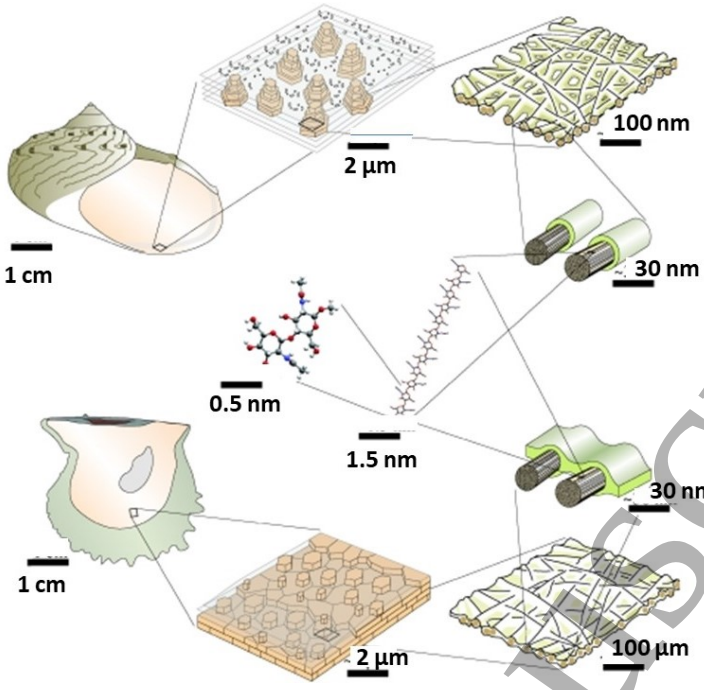

FIG. 2: The nacre (mother of pearl) construction design in gastropod (top) and bivalve molluscs (bottom) is based on a hierarchical architecture ranging from a monomer of the polysaccharide chitin to the whole mollusc shell [3]. (Reprinted with permission from Royal Society Publishing).

growth habit at a macroscopic mm-scale, result from the ordered stacking of virion capsids showing icosahedral symmetry at the ~ 30 nm scale. In turn, these virus particles can be properly regarded as hierarchical macromolecular aggregates themselves. The first two levels are constituted by proteins typically containing 100-200 amino acids, which play the role of basic building blocks. Proteins can appear either single or, more generally, grouped in sets including two, three, four or even more proteins each, to give rise to the so-called protein subunits, generally adopting polygonal shapes. The protein subunits then associate among them to form the third level in the bottom-up structural hierarchy, namely, the capsomers. Within the capsomers, protein subunits can associate in groups of three (trimers), five (pentamers), or six (hexamers) subunits each. Finally, in the fourth hierarchical level, the capsomers organize themselves throughout the space according to pentagonal and hexagonal local patterns, resulting in a virus capsid displaying an icosahedral symmetry as a whole.

Another instance is illustrated in Fig.2, where we see how nacre is built up in a hierarchical fashion from the atomic to the macroscopic scales. In the first stage, chitin monomers

are polymerized, and the resulting polymer chains then crystallize into rod-shaped small crystallites, which ensamble into layers about 100 nm in size. These layers are finally coated in proteins to become membranes which comprise the mortar of the bricks shell's walls [11]. A similar fractal-like hierarchical organization can be observed in bones, extending over twelve levels at least. At a macroscopic level, a bone is composed of two osseous tissue types, namely, cortical (composed of osteon cells) and trabecular bone. Both kinds of tissues are typically made up of lamellae, which are mostly composed of mineralized collagen fibril bundles a few to several micrometres in diameter. The mineralized collagen fibrils, made up of collagen protein fibrils with diameters of the order of approximately 100 nm, and mineral apatite crystal platelets (with hexagonal unit cells, of dimensions $a = b = 9.4$ Å, and $c = 6.8$ Å), are bone's basic building blocks, which assemble hierarchically to provide stiffness (for support and leverage) and toughness (for protection and impact resistance), two properties that are usually considered to be mutually exclusive, but that coexist in bone tissues precisely due to their nested organization [12, 13]. Certainly, the essential role of multi-scale visualization from the very small to the very big can be hardly overemphasized in the exploration of biological phenomena [14].

Remarkably enough, in many biological structures it is not really necessary to explore a very broad scale range to fully appreciate their hierarchical design. For instance, collagen [15] and keratin [16] fibers provide a typical example within the macromolecular scale. By attending to their secondary structure [17] keratin proteins can be classified into α-keratins, which are helical in structure (Fig.3A), and β-keratins which consist of parallel sheets of polypeptide chains (Fig.3B). Based on X-ray diffraction patterns (Fig.3 inset), both show a characteristic filament-matrix structure, where 7 nm (3 nm) diameter intermediate filaments for α (β)-keratin, respectively, are embedded in an amorphous keratin matrix. The α-keratin proteins are organized as coiled coils, consisting of two helically wound chains of polypeptides, each one adopting the α-helix conformation structure, causing the duplex chain to twist and exhibit a helical shape about 2nm in diameter. These dimers then assemble to form the protofilament, and four protofilaments organize into the so-called intermediate filament (Fig.3C), showing an intermediate size (7-10 nm in diameter) between microfilaments (7 nm) and microtubules (24 nm) [18]. For β-keratin, the pleated-sheet arrangement (Fig.3D) consists of laterally packed β-strands which can be parallel or antiparallel (more stable), and the resulting chains are held together by intermolecular hydrogen bonds.

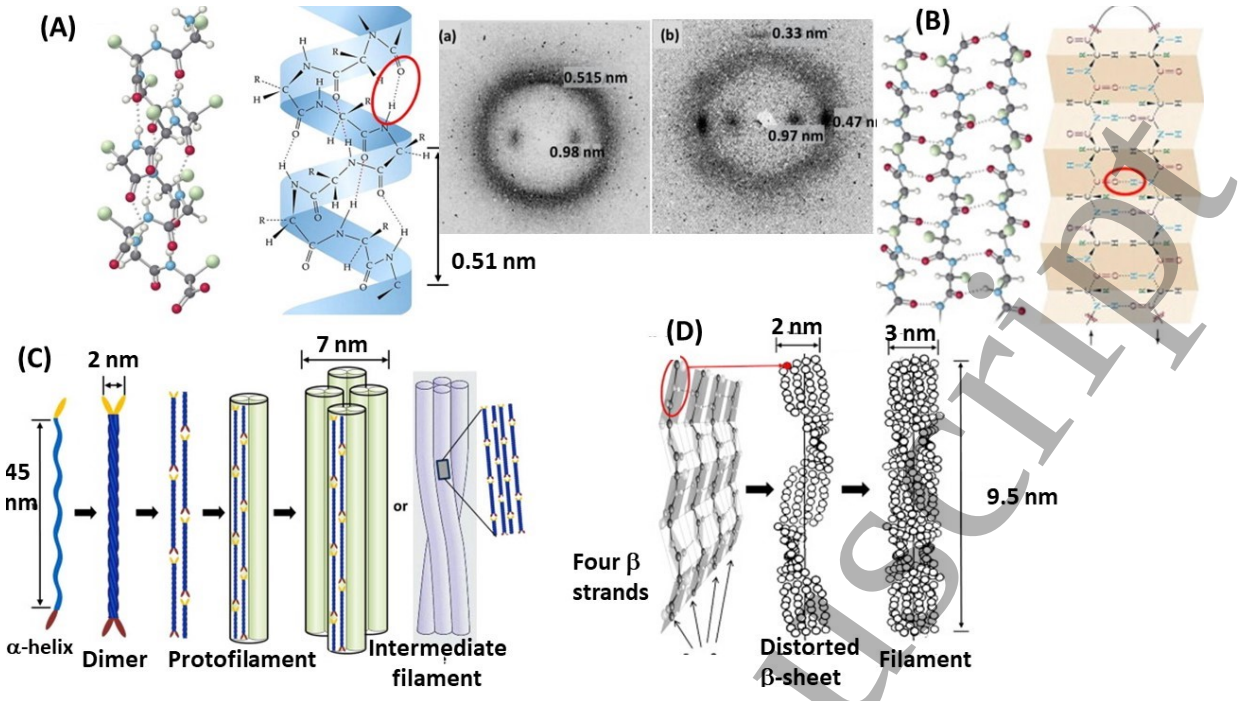

FIG. 3: (A) Ball-and-stick model of the α-keratin polypeptide chain, and α-helix sketch showing the location of the hydrogen bonds (red ellipse) and the 0.51 nm pitch of the helix. Naturally occurring α-helices found in proteins are all right-handed. (B) Ball-and-stick model of the β-keratin polypeptide chain (on the left), and illustration of the pleated β-sheet (on the right). (C) Schematic drawing of the intermediate filament formation (see main text). (D) Schematic drawing of the formation of β-keratin filament: one polypeptide chain folds to form four β-strands which twist to form the distorted β-sheet. Two sheets assemble to form a β-keratin filament. Inset: (a) typical α-keratin bundles X-ray pattern exhibitig an equatorial reflection of spacing of 0.98 nm and a meridional reflection of spacing 0.515 nm; (b) typical β-keratin bundles X-ray pattern with two equatorial reflections of 0.97 nm and 0.47 nm, and a meridional reflection of spacing 0.33 nm [18]. (Reprinted from Progress in Materials Science, **76**, B Wang, W Yang, J McKittrick, M A Meyers, Keratin: Structure, mechanical properties, occurrence in biological organisms, and efforts at bioinspiration, 229-318, Copyright (2016), with permission from Elsevier).

A typical collagen molecule design is illustrated in (Fig.4A), and it consists of three polypeptide chains intertwined in a triple-helix known as tropocollagen, which is then used to make up larger collagen aggregates, referred to as fibrils. A single tropocollagen molecule is approximately 300 nm long and 1.5 nm in diameter, and it is organized in a left-handed

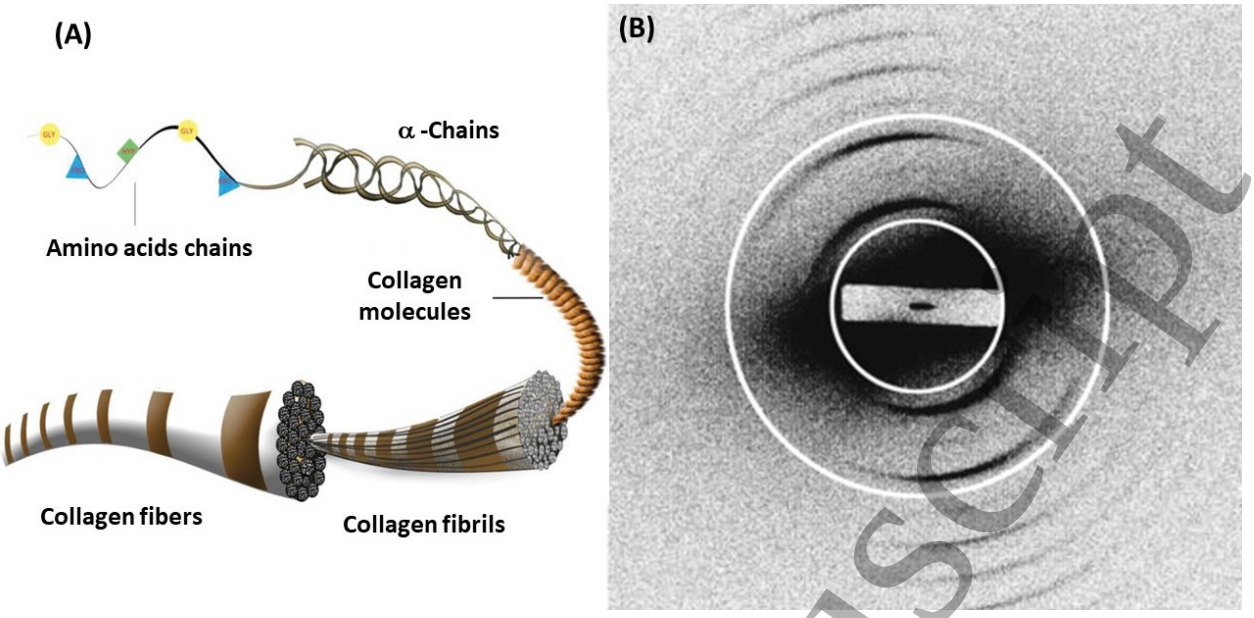

FIG. 4: (A) Sketch of the four level structure of a collagen fiber. Three polypeptides coil to form tropocollagen. Many tropocollagens then bind together to form a fibril, and many of these then form a fibre. In the extra cellular space the molecule is arranged in staggered bundles with a gap of 67 nm by inter molecular bonds tropocollagen units, which gives to the collagen fibril, a repetitive sequence resulting in a characteristic D - banding [19]. (Reprinted from Advanced Functional Matererials, Advanced Collagen Based Biomaterials for Regenerative Biomedicine, K Lin, D Zhang, M H Macedo, W Cui, B Sarmento, G Shen, 2019, **29**, 1804943 © 2018, with permission from John Wiley sons). (B) A representative X-ray diffraction pattern from canine mitral valve collagen. The X-ray beam passed through the sample perpendicular to the plane of the tissue. The pattern is dominated by a series of meridional Bragg reflections, arising from constructive diffraction of X-rays by the regularly repeating 67 nm axial structure of collagen fibrils within the sample [20]. (Reprinted from Biophys. J., 93, M Hadian, B M Corcoran, R I Han, J Gunter Grossmann, J P Bradshaw, Collagen organization in canine myxomatous mitral valve disease: An X-Ray diffraction study, 2472-2476, © (2007), with permission from Elsevier).

secondary structure made up of three polypeptide strands, each of which has the conformation of a α-helix with three amino acids per turn. These three left-handed helices are twisted together into a right-handed triple helix. In most collagen molecules, each triple-helix in turn associates into a right-handed super-super-coil referred to as the collagen microfibril.

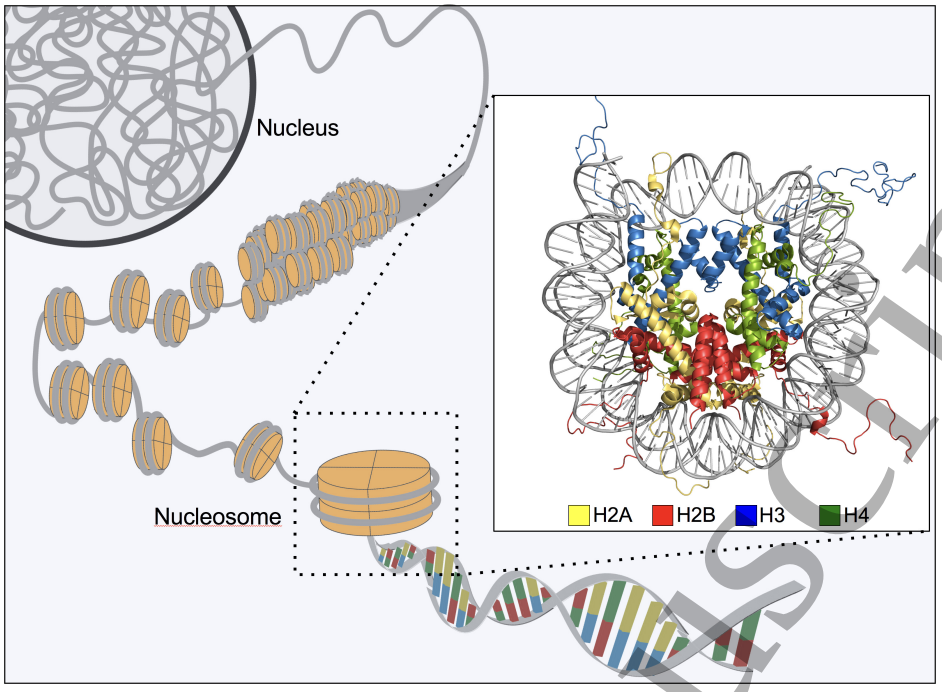

FIG. 5: Hierarchical organization of chromatin at various levels based on nucleosome building blocks [21]. (By courtesy Andrew Scott, Okinawa Science and Technology Institute (OIST), Creative Commons Attribution 2.0 Generic License).

A representative small-angle X-ray diffraction pattern of collagen is shown in Fig.4B. Because collagen fibrils can occur in all possible orientations within this plane, the diffraction pattern exhibits a series of concentric circles, containing information in the meridional plane (describing structure along the axis of the fiber), and in the equatorial plane (describing lateral structure). The ring centered on the middle of the diffraction pattern encompasses the third, fourth, and fifth orders of meridional diffraction.

As a final illustrative example of hierarchical design, now connecting macromolecular and supramolecular domains, let us consider the case of chromatin, which is the name given to the chromosomal material when extracted from the cell's nucleus. It consists mainly of DNA molecules, tightly associated with a number of proteins called histones (Fig.5). The four histones labelled H2A, H2B, H3 and H4 (shown in the inset on the right) are responsible for the first level of structural organization in chromatin, in which short stretches of DNA (147 base pairs long) are wrapped locally around octameric cores of histone proteins, creating compact disk-shaped bodies of 10 nm in diameter referred to as nucleosomes. These

nucleosomes are separated from each other by about 10-50 base pairs chains of unwrapped DNA. A string of nucleosomes made of eight histone proteins is thus created which gives rise to a filament upon packing. To this end, the histone labelled H1 is concerned with the folding of the nucleosome filament into the next higher level of organization, leading to a super-helical double helix , wherein the initial zigzag of nucleosomes loosely connected by relatively short DNA linkers, progressively close up to form helices with increasing numbers of nucleosomes per turn [22]. The placement of nucleosomes along the super-coiled DNA profoundly influences essential DNA interactions, such as gene regulation, transcription, replication, recombination, retroviral integration sites, or DNA repair [23].

II. TILING AND LATTICE MODELS BASED ON BIOLOGICAL PATTERNS AND SHAPES

The biological patterns shown in Fig.6 range in spatial scale from the cm-size to the nm-size, thus sampling a characteristic hierarchical stage in the considered biological system, namely, a sunflower displaying an arrangement of seeds (macroscopic scale, Fig.6A), reticulated vegetal and animal tissues (microscopic scale, Figs.6B-C, respectively), and a virus capsid protein shell (nanoscopic scale, Fig.6D). As we see, the main structural elements present in each representative sample (i. e., seeds, cells and capsomers) exhibit well defined shapes, and they are arranged in well ordered patterns that can be readily described in terms of polygonal tilings or polyhedral packings. Accordingly, the spatial order underlying these structures can be described by means of either tilings or lattice-like geometrical models, which are different, yet closely related mathematical notions. To start with let us consider the sunflower picture showing a tight packing of polygonally-shaped seeds in Fig.6A. Attending to this geometrical arrangement we may describe the seeds pattern as that resulting from a tesselation of a plane disk by more or less regular tiles. A more covenient alternative description considers a number of spiral curves with origin at the disk centre and growing outwards in clockward and counterclockward opposite senses, so that the seeds are located at the interesecting points of the resulting crisscrossings, thereby defining a *spiral lattice* grid. This mathematical description is more adequate because the expanding design of the spiral curve captures the structural consequences of the passage of time in the biological structure in a completely natural way [27]. In fact, our current understanding of botanical

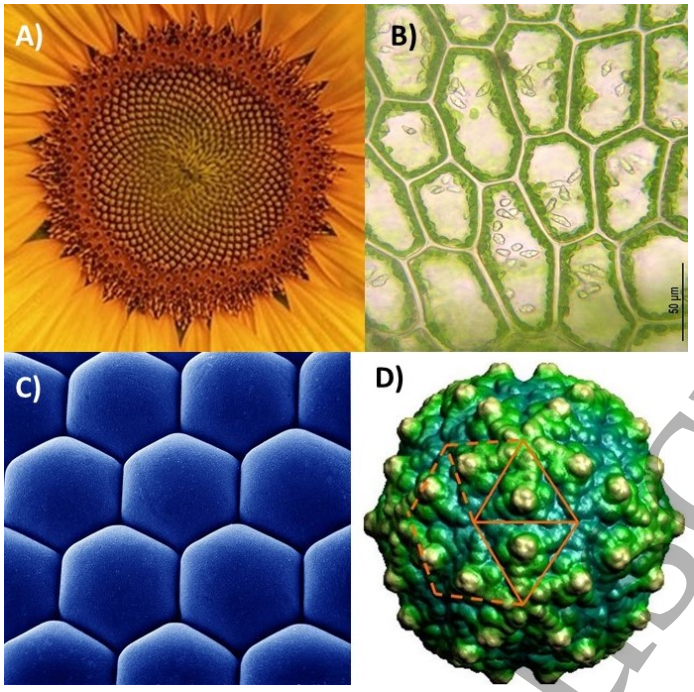

FIG. 6: (A) A sunflower showing spirals of polygonally shaped seeds growing in opposite sense [24]. (B) Calypogeia fissa vegetal tissue showing a tiling made of cells exhibiting polygonal shapes [25]. (C) Honeycomb cell's arrangement in the ommatidia of antarctic krill's eye [26]. (D) Capsid protein structure of flock house virus. Its shape is described by a rhombic triacontahedron, comprised of 30 golden rhombi forming a dihedral angle of $2\pi/5$, which are joined at 60 edges and 32 vertices, of which 12 are 5-fold and 20 are 3-fold ones. (The figure was obtained from VIPERdb (http://viperdb.scripps.edu). [8]).

processes reveals that the architecture of an actual plant is the expression of the ordering displayed as it grows, according to a precise hierarchical unfolding process involving space and time in an intertwined fashion during plant development.

A. Phyllotaxis: A botanically inspired geometry

Phyllotaxis (from the Greek *phýllon* – leaf, and *táxis* – arrangement) describes the helical arrangements of leaves and bracts around the stem of plants, as well as the whorling of sepals, petals, and seeds in flowers. The widespread appearance of ordering patterns based on the Fibonacci series $F_n = \{1, 1, 2, 3, 5, 8, 13, 21, ...\}$ is well established in many botanical patterns

[28]. The terms in this sequence are obtained from the recursive equation $F_{n+1} = F_n + F_{n-1}$, starting with $F_1 = 1$ and $F_2 = 1$, so that each number in the sequence is just the sum of the preceding two. For instance, lilies have 3 petals, buttercups 5, some delphiniums 8, marigolds 13, asters 21, and daisies 34, 55, or even 89 [1]. A similar behavior can be observed in the arrangement of leaves along a tree twig: in elms and basswoods leaves occur alternately on two opposite sides, which is known as a 1/2 phyllotactic ratio. The apple, cherry, oak and apricot have leaves every 2/5 of a turn, the rose, poplar and pear have them every 3/8 of a turn, and the willow and almond exhibit a 5/13 phyllotactic ratio. As we see, all the observed fractions are ratios of either consecutive or alternate terms in the Fibonacci sequence. In a similar vein, the number of intersecting spirals (called parastichies) which can be seen in Fig.6A are generally given by two successive terms of the Fibonacci sequence, say 13 winding clockwise and 21 counterclockwise, a relationship that is referred to as the $(13, 21)$ parastichy index. The parastichy index $(89, 144)$ has been reported in specially large sunflower speciments. In addition to the planar patterns just discussed, phyllotactic patterns involving conical helices revolving in opposite senses in three-dimensional space can be observed in the scales distributions in pineapples and pinecones [29], a description that can be generalized to arbitrary surfaces of revolution. Projecting the cylindrical Fibonacci lattice to the sphere generates its spherical version, which has been used to design golf balls [30], or to optimize measurements in geosciences [31]. In botany spherical Fibonacci lattices are seen in the spatial distribution of spine-bearing nodes of *Mammillaria* cacti [32].

Though Fibonacci based patterns are overwhelming (say, above 90%), there are also phyllotactic patterns in which the number of parastichies on the right and on the left is equal to the neighboring terms of generalized recurrent sequences, such as Lucas numbers $L_n = \{1, 3, 4, 7, 11, 18, 29, \ldots\}$ [33], or even patterns that do not follow any Fibonacci-like recurrence at all, but insted increase almost simultaneously, yielding parastichy numbers of the form (n, n) or $(n, n + 1)$ [34]. Perturbed patterns due to gene mutations have been considered as well [35]. "*Thus we must face the fact that phyllotaxis is really not a universal* law *but only a fascinatingly prevalent tendency*" [36], a tendency naturally expressing the preference of natural processes to add the last two terms together in order to obtain the next one, instead of adding the last three, or four, or more [27].

The phyllotactic ratios previously reported obey a close mathematical relationship with

the golden mean, as prescribed by the asymptotic limit,

$$\lim_{n\to\infty} \frac{F_n}{F_{n-1}} = \tau = \frac{1+\sqrt{5}}{2}, \tag{1}$$

so that the ratio of two successive larger and larger Fibonacci numbers comes closer and closer to the so-called golden mean irrational number, τ. If one considers the ratio between next-neighbors in the Fibonacci series one gets

$$\lim_{n\to\infty} \frac{F_{n+1}}{F_{n-1}} = \lim_{n\to\infty} \frac{F_n + F_{n-1}}{F_{n-1}} = 1 + \lim_{n\to\infty} \frac{F_n}{F_{n-1}} = 1 + \tau = \tau^2. \tag{2}$$

By proceeding in a similar way one can readily see that higher powers of the golden mean are related to asymptotic limits involving ratios of Fibonacci numbers further and further apart along the series. The τ ratio and its related powers are also frequently observed in anatomic branching structures, such as human coronary arteries [37].

The representation of leaves distribution as a point-lattice on a cylinder, representing the unrolled plant stem, was introduced in 1837 by Louis François and Auguste Bravais brothers [38], who later on played a fundamental role in the foundations of classical crystallography as well [39]. They early described phyllotactic patterns in terms of a wound spiral, called the generative spiral. At the center of the plant tip is a small circular region of tissue called the apex, and around this apex form small lumps called primordia, which progessively develop into seeds, petals, leaves, or florets, respectively, as the apex grows away. Therefore, in the reference frame of the tip older primordia are advected away due to the growth while new ones continue to be formed close to the tip [40]. Accordingly, the spiral parastichies we see in Fig.6A are just by-products of the sequence of events that take place during the plant's growing process. In his way, the passage of time is engraved in the structure, and the basic model parameters required to describe the resulting phyllotactic pattern are the so-called *plastochrone ratio*, defined as the ratio of the distances from the centers of two successive primordia to the spiral's origin, and the *divergence angle* introduced by the Bravais as the angle between the new primordium that began to appear at the tip and the primordium that had most recently appeared near the tip [38]. If the divergence angle were a rational multiple of 2π then the seeds would align radially, leaving large empty spaces in between (Fig.7A). Quite on the contrary, in most mature plants this angle is related to the golden mean τ, through the relationship $\phi_d = 2\pi/\tau^2 \simeq 137.51^o$ [28, 41]. The golden mean can be

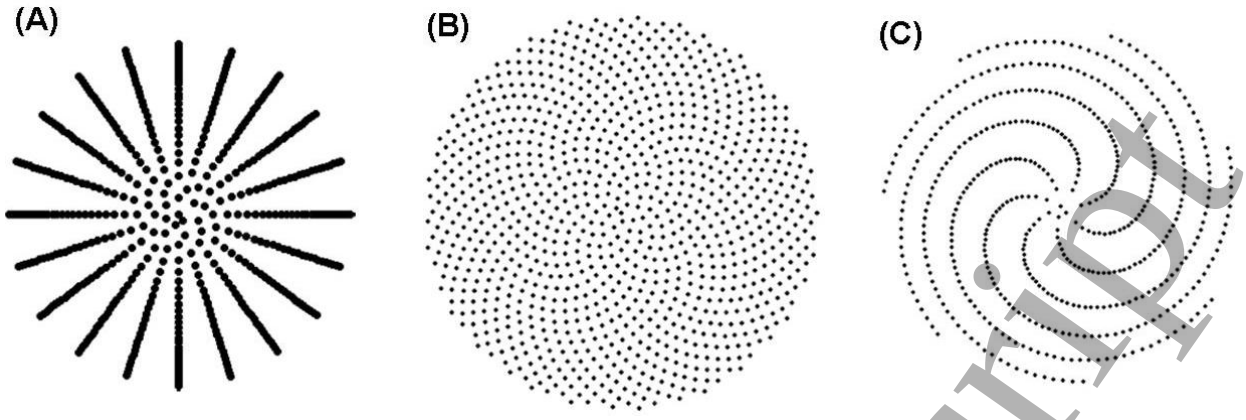

FIG. 7: Phyllotactic patters for different divergence angles: (A) $\phi_d = 3\pi/10$, (B) $\phi_d = \tau$ (1000 seeds), (C) $\phi_d = \pi$ (500 seeds). Note that for a large enough number of seeds the pattern corresponding to (A) displays radial arms exhibiting a $m = 20$ order rotation axis [43]. (M Naylor, Golden, $\sqrt{2}$, and π flowers: A spiral story, 2002 Mathematical Magazine 75, 163-172. Reprinted by permission of Taylor & Francis Ltd.).

expressed as the continued fraction [42, 43]

$$\tau = 1 + \cfrac{1}{1 + \cfrac{1}{1 + \cfrac{1}{1 + \ddots}}}, \tag{3}$$

as can be easily verified by setting the continued fraction equal to some variable, say x, and then recognizing that x is repeated in the denominator of the fractional part in Eq.(3), that is, $x = 1 + 1/x$. This leads to the algebraic equation $x^2 - x - 1 = 0$, whose positive solution is τ. Note that the non-terminating nature of the continued fraction structure is essential to obtain this result, hence providing a nice example of the infinity notion power in mathematical thinking [44]. By inspecting Eq.(3) we realize that τ is the irrational number most badly approximated in terms of rational numbers. In the case of the sunflower inflorescence this property guarantees that the seeds pack together pretty well distributed, so that there is neither crowding at the center nor sparseness at the edges, thereby resulting in very little wasted space (see Fig.7B). Indeed, the distance between neighboring seeds appears to stay nearly constant, hence optimizing the use of the available space. In a similar vein, a golden mean related divergence angle value is very convenient in the arrangement of leaves along the stem, since this ensures that each leaf receives maximum exposure to

light, rain, and insects for pollination, while simultaneously minimizing the probability of obscuring the leaves below at any given stage of growth.

Spiral lattices observed in many botanical structures are based on the application of a simple mathematical algorithm. We start from a generating spiral *curve* in polar coordinates, such as the archimedean, $r = a\varphi$, Fermat (also known as parabolic), $r = a\sqrt{\varphi}$, golden, $r = a\varphi^{1/\tau}$, or logarithmic, $r = ae^{\varphi}$, curves, where $a \in \mathbb{R}^+$. The related spiral *lattice* is then obtained by restricting the possible values of r and φ according to a quantization condition of the form [45, 46]

$$r_n = an^{\nu}, \qquad \varphi_n = \phi_d n, \quad n = 0, 1, 2..., \tag{4}$$

where $\nu \in \mathbb{R}$, and ϕ_d is also a real number measuring the divergence angle between adjacent radius vectors r_n and r_{n+1}. For instance, the so-called Vogel's spirals [47], which describe the arrangement of florets in the sunflower head shown in Fig.6A, are obtained when $\nu = 1/2$ in Eq.(4). This square-root dependence is readily understood by noting that if the florets are assumed to be all the same size and they are densely packed as well, then the total number that can be fitted inside a circle of radius r_n is proportional to its area, hence $r_n \sim \sqrt{n}$. In more realistic descriptions the sizes of the florets increase radially outwards and the generative spiral is the equiangular logaritmic curve [27, 48], whereas the distribution of scales in a pinecone's base essentially obeys an archimedean generative spiral [49].

Spiral lattices provide an interesting instance of ordered systems lacking both translational and orientational symmetries. Instead, they exhibit scale invariance symmetry, a property they share with fractals [50], which is characterized by self-similar inflation or deflation operations. Let S_λ denote the scale transformation operation defined as $S_\lambda f(\mathbf{r}) = f(\lambda\mathbf{r})$, so that a scaling transformation with scaling factor $\lambda \in \mathbb{R}^+$ transforms by λ-multiplication all the components of vector $\mathbf{r} \in \mathbb{R}^N$. Then, the function $f(\mathbf{r})$ is said to be scale invariant when $S_\lambda f(\mathbf{r}) = \mu f(\mathbf{r})$, $\forall\lambda \in \mathbb{R}^+$, where $\mu \in \mathbb{R}^+$. For instance, monomial functions in $\mathbb{R}$, $f(x) = x^n$, satisfy the scale invariance property $S_\lambda f(x) \equiv f(\lambda x) = (\lambda x)^n = \lambda^n f(x)$, where $\mu \equiv \lambda^n$, a relationship characteristic of the so-called homogeneous functions of degree n. By applying this scale transformation to the generating spiral given by Eq.(4), conveniently expressed as $\varphi(r_n) = \phi_d(r_n/a)^{1/\nu}$, we have $S_\lambda\varphi(r_n) = \phi_d(\lambda r_n/a)^{1/\nu} = \lambda^{1/\nu}\phi_d(r_n/a)^{1/\nu} \equiv \lambda^{1/\nu}\varphi(r_n)$. Thus, the original spiral curve is simply scaled by the factor $\mu = \lambda^{1/\nu}$, thereby exhibiting a global scale invariant symmetry.

Taking into account this symmetry the generation of a general phyllotactic pattern can

be modeled in terms of an affine transformation $W:\mathbb{R}^3\to\mathbb{R}^3$ acting on $\mathbf{r}\equiv(x,y,z)^T\in\mathbb{R}^3$ in the form $W(\mathbf{r})=(\mu\mathbf{R})\mathbf{r}+\mathbf{t}$, where μ is a scale factor, $\mathbf{t}\equiv(t_1,t_2,t_3)^T$ is a translation vector, and $\mathbf{R}=\mathbf{R}_{X''}\mathbf{R}_{Y'}\mathbf{R}_Z$ is the blend of the rotation operators [51]

$$\mathbf{R}_X(\alpha)=\begin{pmatrix}1&0&0\\0&c_\alpha&s_\alpha\\0&-s_\alpha&c_\alpha\end{pmatrix},\quad \mathbf{R}_Y(\beta)=\begin{pmatrix}c_\beta&0&s_\beta\\0&1&0\\-s_\beta&0&c_\beta\end{pmatrix},\quad \mathbf{R}_Z(\gamma)=\begin{pmatrix}c_\gamma&s_\gamma&0\\-s_\gamma&c_\gamma&0\\0&0&1\end{pmatrix}, \tag{5}$$

with $c_q\equiv\cos q$ and $s_q\equiv\sin q$, describing counterclock rotations by an angle q around the X, Y, and Z Cartesian axes, respectively [52].

At this point, it is convenient to introduce the Seitz symbol defined in terms of the following block matrix [53]

$$\mathbf{W}=\begin{pmatrix}\mathbf{D}&\mathbf{t}\\\mathbf{0}&1\end{pmatrix}, \tag{6}$$

where $\mathbf{0}\equiv(0,0,0)$, and $\mathbf{D}$ is a 3×3 matrix operator describing symmetries belonging to the point group symmetry (i. e., rotations, scaling, mirror planes, or inversion center operations). The Seitz symbol can be regarded as a 4×4 matrix operator acting upon the auxiliar 4D vector $\mathbf{s}\equiv(x,y,z,1)^T$. Thus, a general coordinate transformation can be written in the form $\mathbf{s}'=\mathbf{W}\mathbf{s}$, which explicitly reads [54]

$$\begin{pmatrix}x'\\y'\\z'\\1\end{pmatrix}=\begin{pmatrix}D_{11}&D_{12}&D_{13}&t_1\\D_{21}&D_{22}&D_{23}&t_2\\D_{31}&D_{32}&D_{33}&t_3\\0&0&0&1\end{pmatrix}\begin{pmatrix}x\\y\\z\\1\end{pmatrix}. \tag{7}$$

Accordingly, pure rotations, pure uniform scaling, and pure translation operations are respectively given by the expressions

$$\mathbf{W_q}\mathbf{s}=\begin{pmatrix}\mathbf{R}&\mathbf{0}\\\mathbf{0}&1\end{pmatrix}\mathbf{s},\qquad \mathbf{W}_\mu\mathbf{s}=\begin{pmatrix}\mu\mathbf{I}&\mathbf{0}\\\mathbf{0}&1\end{pmatrix}\mathbf{s},\qquad \mathbf{W_t}\mathbf{s}=\begin{pmatrix}\mathbf{I}&\mathbf{t}\\\mathbf{0}&1\end{pmatrix}\mathbf{s}, \tag{8}$$

where $\mathbf{I}$ is the 3×3 identity matrix, and the general phyllotactic pattern introduced above can be expressed as

$$\mathbf{W}\mathbf{s}=\begin{pmatrix}\mu\mathbf{R}&\mathbf{t}\\\mathbf{0}&1\end{pmatrix}\mathbf{s}. \tag{9}$$

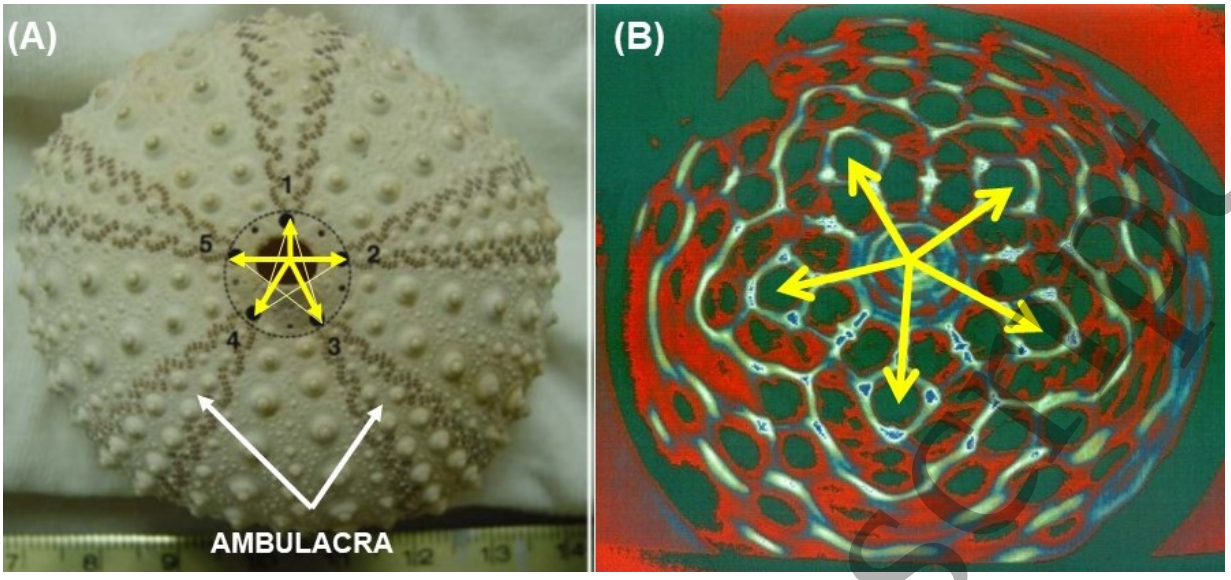

FIG. 8: (A) Aboral surface view of a sea urchine displaying five petaloid ambulacra with the apical disc located in the center of the image. The five optical plates are numbered clockwise, and they define the star vector formed by vectors pointing to these landmarks, with common origin at the center [61] (Reprinted by permission from Springer Nature, Bull. Math. Bio., López-Sauceda, J L Aragón, Eutacticity in sea urchin evolution, Bull. Math. Bio. **70** 625-634, (Copyright) 2008). (B) Nonlinear wave pattern with 5-fold symmetry obtained in the Faraday wave experiments described in the text [55, 77] (Republished with permission of IOP Publishing, Ltd., from The role of aperiodic order in science and technology, E. Maciá, Rep. Prog. Phys. 69, 397, 2006; permission conveyed through Copyright Clearence Center, Inc.). Eutactic stars located in the plane tangent to the aboral surface at the center of the apical disc have been drawn in both pictures.

B. Sea urchins and eutactic stars

Sea urchins are typically spiny, cm-sized globular animals, belonging to the class Echinoidea in the echinoderms phylum. Most regular sea urchins exhibit roughly spherical bodies, displaying a characteristic five-fold symmetry, with five equally sized petal-like features (referred to as ambulacra, see Fig.8A) radiating out from their central axes in the apical disc (encircled in Fig.8A), which is positioned in the aboral surface and is conformed by five genital and five ocular plates, hence rendering a conspicuous sign of pentameric body plan.

This geometrical regularity can be properly measured in terms of the notion of *eutaxy*

(from Greek *eu* – good, and *taxis* – arrangement), which was earlier introduced in the study of the so-called polytopes: geometrical structures that generalize the notions of regular polygons (in 2D), and polyhedra (in 3D), to arbitrary high dimensional spaces [56]. In particular, it was proved that the vectors pointing from the center of any regular polytope to its vertices form a set endowed with very special algebraic properties. In particular, the property of *eutacticity* is described in terms of the so-called *eutactic stars*, which are defined as a set of N vectors sharing a common origin, $\bigstar \equiv \{\mathbf{u}_1, \ldots, \mathbf{u}_N\}$, where each $\mathbf{u}_i \in \bigstar$ belongs to a n-dimensional space with $n < N$. A star of N vectors is said to be eutactic if it can be viewed as a projection of N orthogonal vectors belonging to the higher dimensional space $\mathbb{R}^N$. That is, let $\mathbf{P}$ be a projection operator from $\mathbb{R}^N$ onto $\mathbb{R}^n$, then a star $\bigstar \equiv \{\mathbf{u}_1, \ldots \mathbf{u}_N\}$ in $\mathbb{R}^n$ is eutactic if there exist a series of orthogonal vectors $\{\mathbf{U}_1, \ldots, \mathbf{U}_N\}$ in $\mathbb{R}^N$ such that $\mathbf{u}_i = \mathbf{P}\mathbf{U}_i$, for $i = 1, \ldots, N$. Therefore, the star associated to a regular polytope is eutactic (though the inverse is not necessarily true) [57]. The definition of an eutactic star can be expressed in a more convenient form by introducing an auxiliary $n \times N$ matrix $\mathbf{A}$, whose i-column is formed by the components of $\mathbf{u}_i$ with respect to the standard basis of $\mathbb{R}^n$. Then, the star $\bigstar \equiv \{\mathbf{u}_1, \ldots \mathbf{u}_N\}$ is eutactic if and only if $\mathbf{A}\mathbf{A}^T = \lambda \mathbf{I}$, where $\lambda \in \mathbb{R}$, (if $\lambda = 1$ the star is called normalized eutactic) and $\mathbf{I}$ is the $n \times n$ identity matrix [58]. In the case of planar vector stars, as those shown in Fig.8, the idea is that the five vectors in $\mathbb{R}^2$ can be associated with two vectors in $\mathbb{R}^5$, so that these 5D vectors are orthogonal and have the same norm. In turn, the eutacticity criterion given above can be more suitably expressed by introducing, in the vector space of all $n \times n$ matrices with real entries, the inner product $\langle \mathbf{M}_1, \mathbf{M}_2 \rangle \equiv \mathrm{Tr}(\mathbf{M}_1^T \mathbf{M}_2)$, thereby the angle between both matrices is given by $\cos\phi = \frac{\langle \mathbf{M}_1, \mathbf{M}_2 \rangle}{\|\mathbf{M}_1\| \|\mathbf{M}_2\|}$, where $\|\cdots\|$ stands for the norm induced by the inner product, namely $\|\mathbf{M}\| = \sqrt{\langle \mathbf{M}, \mathbf{M} \rangle} = \sqrt{\mathrm{Tr}(\mathbf{M}^T \mathbf{M})}$. To this end, we define $\mathbf{S} \equiv \mathbf{A}\mathbf{A}^T$, so that the eutacticity criterion can be rewritten in the form [59]

$$\cos\phi = \frac{\langle \mathbf{S}, \mathbf{I} \rangle}{\|\mathbf{S}\| \, \|\mathbf{I}\|} = \frac{\mathrm{Tr}(\mathbf{S})}{\sqrt{n \mathrm{Tr}(\mathbf{S}^2)}}, \tag{10}$$

and the parameter $\varepsilon \equiv |\cos\phi|$ can be regarded as a measure of the eutacticity, where $\varepsilon = 1$ for an eutactic star, and the closer this parameter is to 1, the more eutactic the star is, with a lower bond fixed at $\varepsilon = 1/\sqrt{n}$. Therefore, ε allows one to measure the eutacticity degree of a vector star that is not strictly eutactic. This feature is particularly useful in the study of actual biological samples which can be only approximately described in terms of perfectly

regular geometrical shapes. In particular, the morphological structure of a broad collection of both extant and extinct sea urchins was explored by using Eq.(10) in order to measure their eutacticity degree [60, 61].

Quite interestingly, urchin-like pattern formation can be observed in the study of surface waves on a liquid which are amplified by forcing a vertical oscillatory motion of the container (Fig.8B) [55], so that the effective gravity is periodically modulated according to the expression $g(t) = -g - A\cos\omega t$, where A and ω are the driven amplitude and frequency, respectively. As soon as the driving amplitude exceeds a critical threshold A_c a standing-wave instability occurs with temporal frequency $\omega_0 = \omega/2$. The standing-wave pattern is determined by the gravity-capillary dispersion relation of the fluid

$$\omega_0^2 = gk_0 + \frac{\sigma k_0^3}{\rho}\tanh(k_0 h), \tag{11}$$

where $k_0 = 2\pi/\lambda_0$, σ is the surface tension, ρ is the fluid density, and h is the liquid depth. Depending on the driven frequency and fluid properties, several symmetries can be observed in the resulting patterns, the most usual ones being parallel stripes and square patterns. More unusual patterns, including octagonal, dodecagonal, and pentagonal symmetries have been reported [55, 62, 63] and theoretically discussed [64, 65]. The pattern shown in Fig.8B was obtained in a circular vessel under free boundary conditions. Remarkably enough, some of the five-fold patterns observed in these experiments resemble the evolutionary sequence of some sea urchins as purported by paleontological fossil records (Echinoids have a rich fossil record dating back to the Ordovician, some 450 million years ago), hence suggesting a possible mechanism for inducing the pentagonal symmetry observed in the early development of these animals [66, 67].

C. The geometry of cell arrangements in tissues

The quantification of the spatial order of the arrangement of cells in tissues, such as those shown in Fig.9, is usually characterized by methods based on: 1) the number of sides of polygonal (polyhedral) cells, 2) the cellular coordination number at the mosaic vertices, 3) the angles defined by the adjacent cells at the vertices, 4) the cell areas (volumes), 5) the average nearest heighbors distances among the cell's centers, and 6) the polygonality index, which measures how far a given test polygon is from a regular polygon's shape with

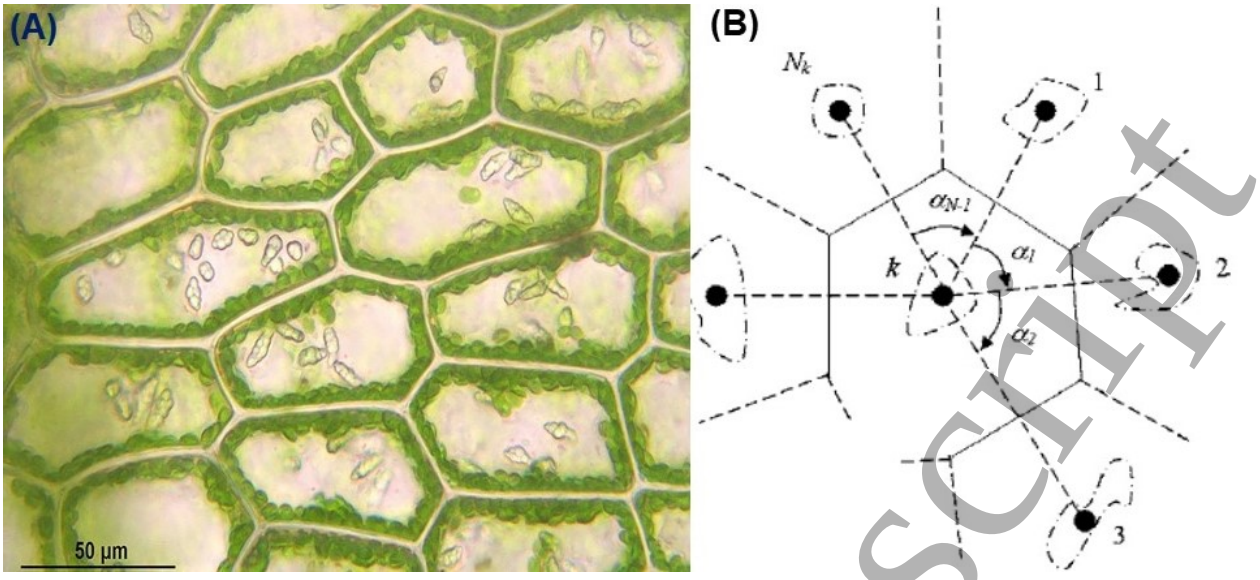

FIG. 9: (A) Calypogeia fissa vegetal tissue showing a tiling made of cells exhibiting polygonal shapes [25]. (B) The geometrical construction and symbols used in the definition of the poligonality index. The reference points are shown as black dots, and the neighbors of seed k are enumerated in a clockwise fashion from 1 to N_k [68]. (Reprinted figure with permission from L Costa, F Rocha, S Lima, Physical Review E, **73**, 011913, 2006. Copyright (2006) by the American Physical Society).

interior angle β. For the sake of illustration, let us consider the geometrical tiling defined by the cells' membranes in the vegetal tissue shown in Fig.9A. For any given cell, say k, we pinpoint the N_k succesive neighbors around it in a clockwise sense, measuring the angles α_i determined by the adjacencies (see Fig.9B). Then, the polygonality index of the test cell is defined as [68]

$$\Delta_\alpha(k) = \frac{1}{1 + \sum_{i=1}^{N_k} |\alpha_i - \beta|},$$

whose value ranges from 1, for perfect poligonality, to negligible small values for a complete lack of spatial order. Alternatively, the measure of regularity in polygonal mosaics of different kinds of biological systems can be performed by averaging the eutacticity degree of the different cells in a given tissue [57].

Voronoi tessellations have also been extensively used to model the geometric arrangement of different biological systems, such as the distribution of cells in both healthy and cancerous tissues [70], or the phyllotactic pattern of seeds in flowering plants [71]. A Voronoi tessellation is the partitioning of a plane with n arbitrarily ordered points into convex polygons

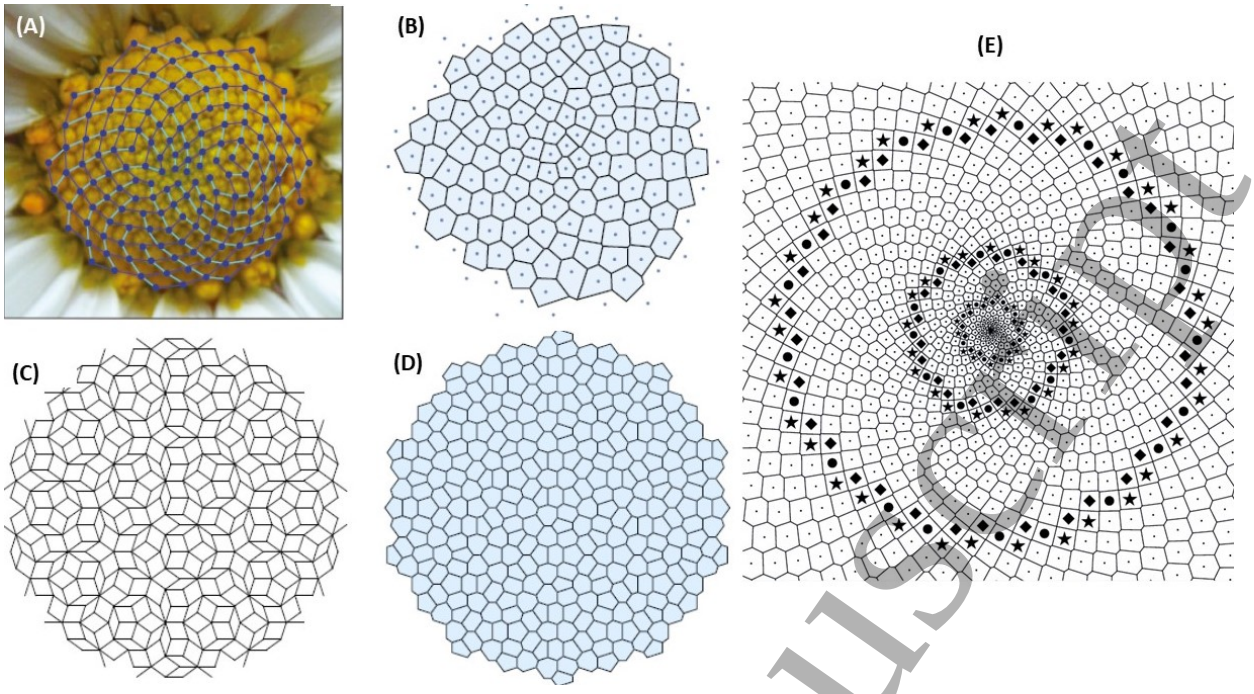

FIG. 10: (A) A flower (Leucanthemum maximum) showing the spiral phyllotactic pattern, (B) Voronoi tesselation associated to the set of points given by the florets centers, (C) fragment of a quasiperiodic Penrose tiling exhibiting 5-fold rotational and scale invariance symmetries, and (D) its related Voronoi tesselation [57]. (C Contreras-Figueroa, L Hernández-Sandoval, J L Aragón, A measure of regularity for polygonal mosaics in biological systems, Theor. Biol. Med. Model. 2015, **12**, 27, doi: 10.1186/s12976-015-0022-1, CC Attribution license 4.0). (E) Voronoi tiling for an Archimedean spiral lattice. The mark ♦ denotes a heptagon, • a hexagon, and ★ a pentagon. The other tiles are hexagons [69]. (Y Yamagishi and T Sushida, Archimedean Voronoi spiral tilings, J. Phys. A: Math. Theor., 51, 045203, 2018; DOI 10.1088/1751-8121/aa9ada/meta; © IOP Publishing. Reproduced with permission. All rights reserved).

such that each polygon contains exactly one generating point and every point in a given polygon is closer to its generating point than to any other. The geometrical tiling defined by the cells' membranes in the muscle tissue shown in Fig.9B roughly conforms to the Voronoi tessellation related to the cell's nuclei spatial distribution. Some additional examples are shown in Fig.10. As we see, because Voronoi polygons have a number of sides equal to the number of nearest neighbors of the point in the center, they readily allow the quantification of the deviation from the ideal regular geometry [72]. Hence, Voronoi tessellation can be

successfully used to identify lattice defects. For instance, the phyllotactic structure shown in Fig.10E consists of hexagonal cells contained in concentric circular rings of increasing radius value, bounded and separated by circular grain boundaries made of F_n heptagonal cells (inner ring), F_{n-1} hexagonal cells (middle ring), and F_n pentagonal cells (outer ring) [73]. With reference to a perfect hexagonal 2D lattice pentagons and heptagons are disclination deffects of opposite weights, whereas a pentagon-heptagon pair gives rise to a dislocation in the Voronoi cell pattern.

III. THE APERIODIC CRYSTALS REALM

"In physics we have dealt hitherto only with periodic crystals. To a humble physicist's mind, these are very interesting and complicated objects; they constitute one of the most fascinating and complex material structures by which inanimate nature puzzle his wits. Yet, compared with the aperiodic crystal, they are rather plain and dull" Erwin Schrödinger, 1944 [74].

To the best of my knowledge, the aperiodic solid notion was introduced by Erwin Schrödinger in 1944, in order to account for the possible nature of the genetic material. In fact, during the 1940s DNA was regarded as a periodic tetranucleotide macromolecule, say $(\mathrm{ACTG})_n$, where the letters A, C, T and G respectively stand for adenine, cytosine, thymine and guanine nucleotides, and as such, unable to store the amount of information required for the governance of cell function. At variance with this view, Schrödinger suggested that a gene consists of a long sequence of a few repeating elements exhibiting a well defined order *without* the recourse of periodic repetition. In this way, the notion of a one-dimensional *aperiodic crystal* was originally introduced by considering that DNA was able to store the required genetic information in just the precise alternating way the four different kinds of nucleotides are arranged throughout space, thereby lacking the previously assumed trivial periodic order [74]. On the basis of detailed X-ray diffraction studies it was subsequently realized that, from a structural point of view, DNA fiber crystals could be classified as a periodic crystal with helical symmetry if one attends to the sugar-phosphate scaffold exclusively, but they could be properly regarded as aperiodic solid representatives if we focus on the nucleobase system *electronic structure* instead (Fig.11). In fact, along with a periodic atomic arrangement in the sugar-phosphate DNA backbone, one also has an

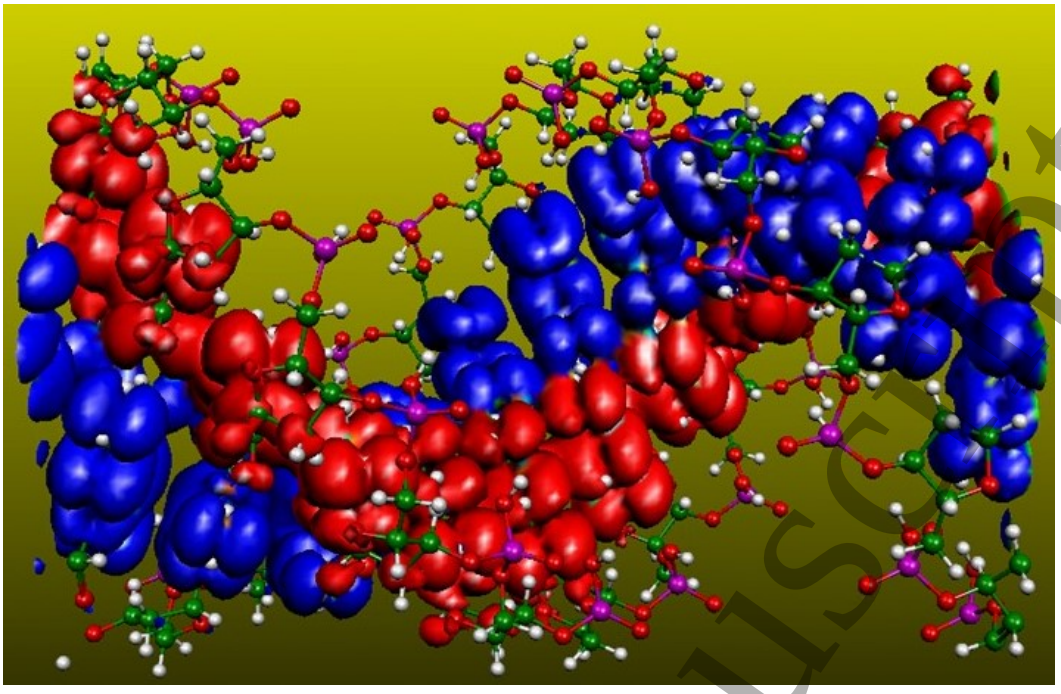

FIG. 11: A view of DNA aperiodic solid at the molecular orbital scale is illustrated by surfaces of constant charge density for the states corresponding to the lowest unoccupied band and highest occupied bands of a short DNA molecule in the A form in dry conditions [75]. These molecular orbitals are related to the guanine (in blue) and cytosine (in red) nucleobases located in the core of the double-helix structure, and around them we can see the atoms belonging to the outer sugar-phosphate backbone (Courtesy of Emilio Artacho).

aperiodic distribution of informative chemical order at the molecular scale, as determined by the base pairs sequence along the double-helix axis. The chemical order of the base pairs sequence itself is beyond the reach of diffraction techniques, but it can be properly characterized via *ab-initio* quantum chemistry calculations, which nicely highlight the emergence of molecular orbitals when going from the atomic to the molecular scale. Accordingly, one may think of DNA as a sort of hybrid order system exhibiting both aperiodic (nucleobase subsystem) and periodic (sugar-phosphate backbone double-helix subsystem) order features [76].

Thus, the DNA case conveniently illustrates our main point: in the conceptual route leading from a QP *lattice* to a QP *solid* we must endow lattice points with both physical (mass, size, charge, spin) and chemical (s, p, d, or f nature of electronic states; ionic,

covalent or metallic nature of bonds) attributes, and properly incorporate these ingredients in a Hamiltonian model relating the underlying geometrical order of the QP lattice point to the resulting physical and chemical properties of the related QP solid. In this way, a key question in the theory of aperiodic crystals, regarding the relationship between their atomic spatial order, determined by a given aperiodic distribution of atoms and bonds all over space, and the physical properties stemming from the resulting physicochemical network could be properly addressed [50].

By closely inspecting the biological structures shown in Figs.1-10 we realize that, with the only exception of the krill's eye ommatidia (showing a neat hexagonal periodic lattice; see Fig.6C), all of them display a patterned aperiodic order instead. Etymologically aperiodic order means *order without periodicity*, hence encompassing those matter arrangements which exhibit well-defined long-range spatial correlations beyond mere periodicity [77]. This property clearly distinguishes aperiodic structures from amorphous matter, which only displays short-range correlations (if any). In this context it is convenient to highlight that, although both random structures and aperiodically ordered arrangements lack strict *translational* symmetry, the *absence of periodicity* characteristic of aperiodic systems is not the same in nature as the *complete lack* of *long-range order* characteristic of amorphous matter. In fact, in aperiodic systems translational symmetry is usually replaced by other symmetry properties which amorphous matter does not possess. Accordingly, arrays of atoms in aperiodic crystals are able to give rise to high quality X-ray or electron diffraction patterns composed of a collection of discrete Bragg reflections, just as periodic arrays of atoms do in classical crystals. Therefore, aperiodic order has nothing to do with disorder in any of its possible multiple forms.

Thus, the International Union of Crystallography (IUCr) approved in April 1991 the establishment of a *Commission on Aperiodic Crystals* to promote the development of common methods and nomenclature for the crystallographic investigation of aperiodic crystals. According to the terms of reference introduced by this Commission:

> *In the following, by "crystal" is meant any solid having an essentially discrete diffraction diagram, and by "aperiodic crystal" is meant any crystal in which three dimensional lattice periodicity can be considered to be absent* [78].

The revamped crystal definition highlights that periodicity at the atomic scale is a suf-

ficient but *not necessary* condition for crystallinity. Instead, the presence of a long-range atomic order *able to diffract* must be regarded as the essential attribute of crystalline matter. Consequently, within the crystalline family we can now distinguish between periodic crystals, which display periodic arrangements of atoms, and aperiodic crystals, lacking such a periodicity, which is replaced by other kinds of symmetries, such as scale invariance (inflation symmetry) or long-range repetitiveness. Therefore, the existence of a mathematically well defined long-range atomic order should be properly regarded as the *generic* attribute of ordered solid state matter.

To date the existence of aperiodic crystals has been reported in three broad classes of materials, namely, incommensurate composites, incommensurately modulated phases, and quasicrystalline compounds [79–81]. In all of these structures the atomic arrangements exhibit well defined long-range order, which gives rise to high quality discrete diffraction patterns, in spite of the absence of lattice periodicity. A characteristic feature of these diffraction patterns is that the positions of the obtained Bragg reflections can be properly indexed by a suitable generalization of the classical Miller's indices in the form:

$$\mathbf{H} = \sum_{i=1}^{N} h_i \mathbf{a}_i^*, \quad N \geq 3, \tag{12}$$

where $\mathbf{a}_i^*$ and h_i are the basis vectors of the reciprocal lattice and integer coefficients, respectively, and the number N is the minimum integer for which the positions of the peaks can be described with integers coefficient h_i. In the case $N = 3$ we have a periodic crystal, whereas when this number is greater than the dimensions of the physical space we are dealing with an aperiodic crystal instead.

An important distinction can be made between incommensurate structures and quasicrystals (QCs) by attending to their X-ray, electron or neutron diffraction patterns [82], namely: for incommensurate structures one can always find a sub-pattern of high intensity spots (the so-called main reflections), related to an average periodic structure in physical space. Along with these high intensity reflections, there is a set of lower intensity peaks grouped around them (the so-called satellite spots). Taking into account these satellite reflections the diffraction pattern becomes $3 + d$ dimensional, where d is the number of satellite *directions*. The most common form of modulated aperiodic crystals display satellites aligned in only one direction ($d = 1$) on either side of the main reflections, so that the diffraction pattern

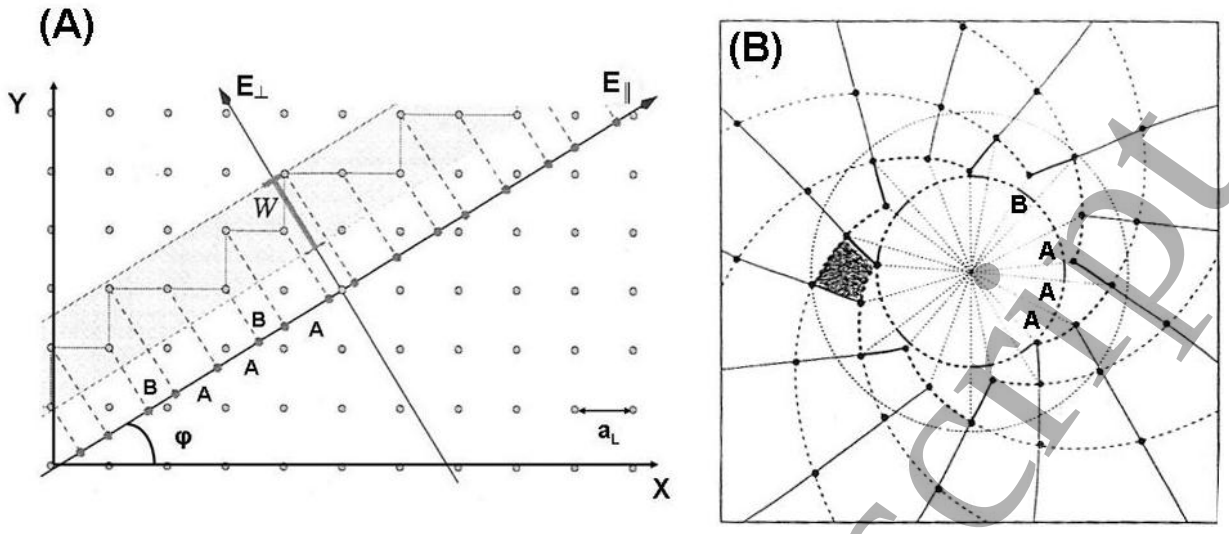

FIG. 12: (A) Construction of the 1D Fibonacci lattice through the cut-and-project method. The slope of the $E_{\parallel}$ axis equals the reciprocal of the golden mean ($\tan\varphi = \tau^{-1}$). In this diagram the projection window W defines the so-called acceptance domain, since only those lattice points inside the strip of width W are projected onto $E_{\parallel}$ (dashed lines). (B) A spiral pattern with phyllotactic index (8,13). The lattice points contained inside the concentric annulus (circular dashed and dotted lines) are radially projected onto the center (dotted radial lines), thereby intersecting the inner circle in a series of long (A) and short (B) arcs arranged according to the Fibonacci sequence.

can be indexed by the introduction of a single reciprocal vector $\mathbf{q} = \alpha\mathbf{a}^* + \beta\mathbf{b}^* + \gamma\mathbf{c}^*$, such that the diffraction vectors $\mathbf{H}$ take the form

$$\mathbf{H} = h\mathbf{a}^* + k\mathbf{b}^* + l\mathbf{c}^* + m\mathbf{q}, \tag{13}$$

where m indicates the number of multiple reflections [83]. The satellite reflections stem from the presence of structural modulations characterized by a periodicity which is incommensurate with that of the average structure. Usually the amplitude of this modulation is relatively small, so that the overall structure can be confidently described in terms of a perturbed averaged periodic structure.

On the contrary, there is no periodic reference structure in QCs, and their structure determination is more demanding in this case [84]. According to its earlier definition a QC is the natural extension of the notion of a crystal to structures with *quasiperiodic*, rather than periodic, translational order [85]. A function f on $\mathbb{R}$ is quasiperiodic (QP) if for some

positive integer $n \geqslant 2$ there exists a continuous function Q on $\mathbb{S}^n$, where $\mathbb{S}$ is the unit circle $[0, 2\pi)$, and a frequency vector $\omega = (\omega_1, \cdots, \omega_n)$, such that $f(x) = Q(x\omega_1, \cdots, x\omega_n)$. A simple one-dimensional example of a QP function is given by $f(x) = A_1 \cos(x) + A_2 \cos(\alpha x)$, where α is an irrational number and A_1 and A_2 are real numbers. Remarkably enough this QP function can be written as a one-dimensional *projection* of a the *periodic* function in *two* dimensions $f(x, y) = A_1 \cos x + A_2 \cos y$, through the restriction $y = \alpha x$. Since any QP function can be thought of as deriving from a periodic function in a space of higher dimension, the so-called cut-and-project method, which is widely used in the study of QCs, ultimately relies on this mathematical property. In this way, most of the basic notions of classical crystallography can be properly extended to the study of QCs by considering suitable lattices in appropriate hyperspaces.

In order to illustrate the essential features of the cut-and-project method let us consider the square lattice of points shown in Fig.12A, having integer Cartesian coordinates (n_x, n_y), playing the role of a 2D hyperlattice with a unit cell parameter a_L. Rotated by an angle φ with respect to the square lattice coordinate system XY, we introduce another orthogonal coordinate system with axes labeled $E_\parallel$ and $E_\perp$. The orthogonal projection of the square lattice points contained within a strip window of width W onto the physical space line $E_\parallel$ determines an aperiodic squence of line segments of different length between successive points, which are labelled A (long) and B (short), respectively. Only in the case of $\tan\varphi$ being a quadratic irrational number will this sequence of segments be a QP one, otherwise, it will be periodic instead. A completely analogous procedure can be used in the case of 2D phyllotactic patterns defining a spiral lattice as that shown in Fig.12B, though in this case instead of a linear strip acceptance domain we employ a circular annulus in order to obtain the corresponding radial projections [86].

As a consequence, QCs display long-range orderings of atoms through the space which can be properly described in terms of a systematic application of inflation symmetry operations. Indeed, the presence of the scale invariance symmetry is essential to obtain a QP translation order [79, 81]. This symmetry had not been previously considered in classical crystallography, and it is directly related to the emergence of self-similar, hierarchical patterns embodying atomic cluster aggregates. Therefore, from a structural viewpoint QCs can be regarded as self-similar arrays of atoms, where the translation symmetry, characteristic of periodic crystals, is *replaced* by a scale invariance one, with scale factors given by *irrational*

numbers. In summary, the three classes of aperiodic crystals identified up to now share a common feature, namely, all of them exhibit order without translational symmetry [87]. In addition QCs differ from incommensurate phases by the fact they also exhibit a novel crystallographic symmetry: scale invariance [81, 88, 89].

As we have pointed out above, the complex structures usually studied in biology are mostly aperiodic in nature. Does this imply that they could be properly regarded as aperiodic crystals? and, if so, which ones (if any) could be properly classified as QC representatives? Regarding the first question, on the one hand, we must distinguish between macromolecular (such as DNA molecules and protein complexes) or supramolecular (e. g., protein and virus crystals) condensed matter phases, and cellular ensembles in biological tissues, on the other hand. For one thing, the existence of a number of protein based aperiodic crystals, belonging to the incommensurate modulated phase class, has been well documented from the detailed study of their obtained X-ray diffraction data during the last decade [90–94]. On the contrary, the possible application of diffraction techniques to characterize the order underlying in biological tissues is a delicate issue. Certainly, it is possible to generate photon density waves with wavelength below 5 cm in these samples. Within the 700-1300 nm wavelength range those photons penetrate multiple centimeters through living intact tissue, and can provide direct measurements. The deeper penetration occurs within this optical window due to relatively weak absorbance of photons by the primary chromophores in biological tissue (i. e., water, lipids, and hemoglobin). When this kind of waves encounter optical inhomogeneities with diameters in the millimeter and centimeter range, typical scattering effects occur at regions with different absorption and scattering coefficient [95] (a similar effect can be obtained by using ultrasound waves instead). Importantly, though the photon absorption is low, the scattering of photons is high in biological tissue and can be well approximated as a diffusive process which is successfully exploited in the so-called diffuse optical tomography techniques [96]. Nevertheless, no scattering centers analogous to atoms in both inorganic and organic compounds can be easily identified in biological tissues, so that the current IUCr crystal definition is not readily applicable to these materials in its present form.

A possible way to circumvent this shortcoming may be to exploit some of the geometrical procedures described in Sec.II C in order to map the actual distribution of cells in a given tissue onto a suitable lattice-like pattern (see Fig.10B,E), and then study the diffraction

properties of this related latticed-point set. In turn, the required mapping may be produced either on purely mathematical grounds (e. g., numerical diffraction calculations on a computer) or by using a physical realization of the lattice-point structure (e. g., by means of 3D laser printers), and then performing optical or acustical diffraction measurements in the resulting structures. For example, optical diffraction has been successfully employed as a tool for quantitative analysis of tissue speciments on the basis of illuminating previously obtained transparent micrographies by a laser beam, which is then diffracted to get the diffraction pattern [97]. The Fourier analysis of the cell shapes has been also reported by using this technique [98].

Regarding the second question above, the phyllotactic patterns displayed by most botanical arrangements described in Sec.II A, could be properly considered as QC representatives, since the related generative spiral exhibits a global scale invariance symmetry with a scale factor that is not rational in most studied botanical systems. In fact, as we saw, when the divergence angle is a rational number, say $\phi_d = q_n/p_n$, with q_n and p_n coprime integer numbers, then one obtains regular periodic patterns for a large enough number of elements in the considered system (Fig.7A). In that case, the Fourier transform of the spiral lattice will show up a discrete collection of Bragg reflections in the reciprocal space, the overall pattern displaying a rotational symmetry corresponding to an order p_n. In general, this number will not belong to the set $\{2, 3, 4, 6\}$, listing the rotation symmetries allowed in classical crystallography according to the so-called restriction theorem. This is a feature that general spiral lattices share with most QCs reported to date in both metallic alloy systems and soft matter representatives [81]. Now, if we instead adopt irrational values for ϕ_d, we then obtain lattices entirely lacking rotational symmetry (Fig.7B-C). Accordingly, their diffraction patterns do not show sharp reflection spots, but rather they feature broad patchy rings, whose spectral features are determined by the particular spiral lattice geometry [49, 99].

For the sake of illustration, in Fig.13a we show the Vogel spiral lattice derived from the Cartesian coordinates expression

$$x_n = a\sqrt{n}\cos(n\phi_d), \;\; y_n = a\sqrt{n}\sin(n\phi_d), \tag{14}$$

where $a \in \mathbb{R}^+$ is a scaling factor and $\phi_d = 2\pi/\tau^2 \simeq 137.508^o$ is the golden angle divergence angle. The calculated and experimental diffraction patterns are shown in Fig.13c and 13d, respectively. A close inspection of these diffraction patterns reveal a finer structure in the

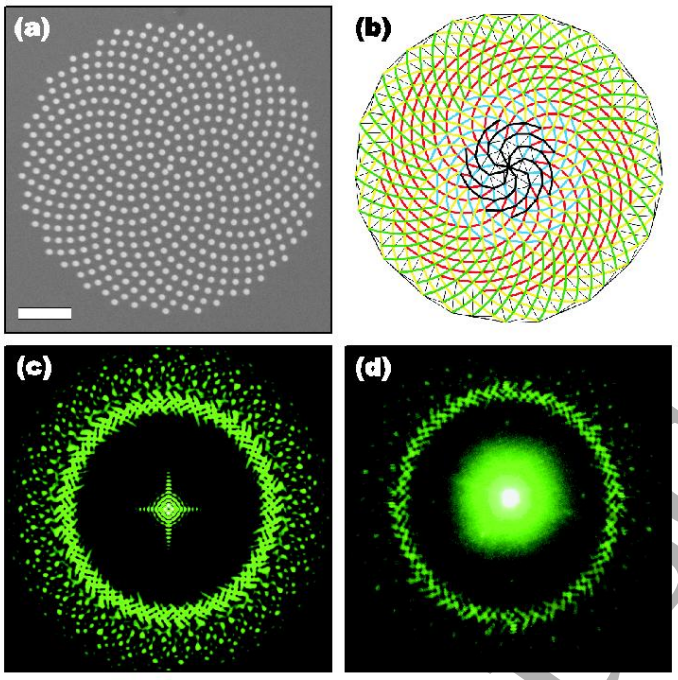

FIG. 13: (a) Scanning electron microscope image of a sunflower fabricated by electron beam lithography containing 500 holes of radius $r = 0.539$ μm. The pattern, displaying the characteristic parastichies spiral curves, has a strong modal nearest-neighbor pitch $d = 2.2$ μm derived from a Delaunay triangulation of the points set shown in (b). The calculated and experimental optical diffraction patterns are shown in (c) and (d), respectively, where the circular ring feature has an average radius of 0.45 $(\mu\text{m})^{-1} \simeq d^{-1}$ [100, 101]. (Republished with permission of IOP Publishing, Ltd., from Exploiting aperiodic designs in nanophotonic devices, E. Maciá, Rep. Prog. Phys. 75, 036502, 2015; permission conveyed through Copyright Clearence Center, Inc.).

main concentric ring, along with the presence of a number of discrete outer Bragg reflections around it. These outer reflections display a spiral structure resembling the parastichies distribution of the sunflower spiral lattice shown in Fig.13a [100]. Using analytical Fourier-Hankel decomposition it was found that the Fourier transform of a Vogel spiral density given by

$$\rho(r,\varphi) = \sum_{n=1}^{N} \frac{1}{r}\delta(r - a\sqrt{n})\delta(\varphi - n\phi_d), \tag{15}$$

can be written as [102],

$$F_m(k_r) = \frac{1}{2\pi}\sum_{n=1}^{N} J_m(k_r a\sqrt{n})e^{inm\phi_d}, \tag{16}$$

which describes the diffraction spectrum of Vogel spiral arrays with an arbitrary divergence angle ϕ_d, where $k_r = 2\pi q_r$ is the radial wave vector associated to the radial spatial frequency q_r, and J_m is the m-th order cylindrical Bessel function of the first kind. The key result is that the exponential factor in Eq.(16) will contribute with azimuthal peaks when the product $m\phi_d$ is an integer. Since ϕ_d is an irrational number this will never occur exactly, but the situation can be reasonably fulfilled by the rational approximants of $\phi_d \simeq q_n/p_n$. Therefore, for spirals generated using an arbitrary irrational number ϕ_d relatively strong azimuthal Bragg reflections of order p_n will appear in the Fourier spectrum due to the denominators of these rational approximants [102]. As we see, Vogel's spirals with remarkably different structures can be obtained by choosing slightly different values of ϕ_d, hence providing a suitable design parameter to control different degrees of aperiodic structural complexity [103].

Thus, if we define QCs as aperiodic structures characterized by the simultaneous presence of both rotation and inflation symmetry operations in their spatial structure, spiral lattices can not be strictly regarded as a QC, since they lack rotational symmetry [100]. However, by inspecting Fig.12B we readily realize that phyllotactic spiral lattices can be straighforwardly related to a QP distribution of seeds via a suitable cut-and-project method [45, 86, 104, 105], hence strongly indicating that these arrangements should be properly regarded as QCs. Yet, we should classify *phyllotactic QCs* as belonging to a different class, since they completely lack rotational symmetries, at variance with QCs reported to date in both alloy systems and soft matter arrangements [50, 81], most of them exhibiting 5-fold, 8-fold, 10-fold, or 12-fold rotational symmetries [106]. In fact, it should be noted that the very existence of phyllotactic QCs was put forward before the discovery of intermetallic ones, as a natural mathematical consequence of imposing radially self-similar symmetry along with local homogeneity to a Voronoi lattice [45]. On the other hand, it has been suggested that the lateral organization of collagen fibrils shown in Fig.4A may be described as a dense packing of more-or-less parallel rods which may adopt a spiral phyllotactic pattern as a whole [73], and a possible relation between the so-called Boerdijk-Coxeter helix [107, 108], a polygonal helix derived from a linear stacking of regular tetrahedra, and α-helix based collagen proteins was discussed within the context of the characteristic QCs' scale invariance symmetry [109]. Indeed, the presence of Bragg reflections in the X-ray diffraction patterns of both keratin (Fig.3 inset) and collagen (Fig.4B) fibers, indicates that these biological structures may be regarded as

crystals according to the revamped IUCr definition. Now, in order to properly classify them as aperiodic crystals we should eliminate the possibility of any possible periodic indexation scheme in the obtained diffraction patterns. In this regard, some ambiguities have been reported in the diffraction patterns of collagen fibrils, both along the molecules and in the perpendicular plane, strongly suggesting a QP structure in both directions, with a scaling factor close to $1 + \sqrt{3}$ [110].

IV. SYMMETRY PRINCIPLES IN VIRUS ARCHITECTURES

Symmetry is commonly exploited by Nature to build up biomolecules with specific shapes. For example, as we have seen in previous sections, helical symmetries are used to create filaments and fibers, whereas icosahedral group symmetries are usually found in nanocontainers, such as virus particles [111]. Viruses can be regarded as condensed soft matter representatives located at the borderline between supramolecular complexes and supercluster atomic aggregates ultimately leading to the formation of biological crystals (Fig.1). The first virus to be discovered (in 1892) and subsequently crystallized (in 1935) was the tobacco mosaic virus (TMV), followed by tomato bushy stunt virus (TBSV; crystallized in 1936), and the turnip yellow mosaic virus (TYMV), which crystallizes from salt solutions as isotropic octahedra. Poliomyelitis virus was the first animal crystal virus, grown in 1955.

In 1956 Francis H. C. Crick and James D. Watson suggested that most virus capsids could be built up from a relatively small number of protein subunits arranged in a highly symmetrical way [112]. The first experimental evidence confirming icosahedral symmetry in a virus came from the X-ray diffraction studies of Donald L. D. Caspar on TBSV [113], along with those by Aaron Klug and Rosalind E. Franklin on TYMV [114]. These investigations confirmed that the X-ray diffraction patterns from certain virus crystals showed intensity distributions characteristic of a periodic arrangement of icosahedral particles throughout the space, and it was concluded that icosahedral virus capsids are structured according to a hierarchical modular design architecture (see Fig.1).

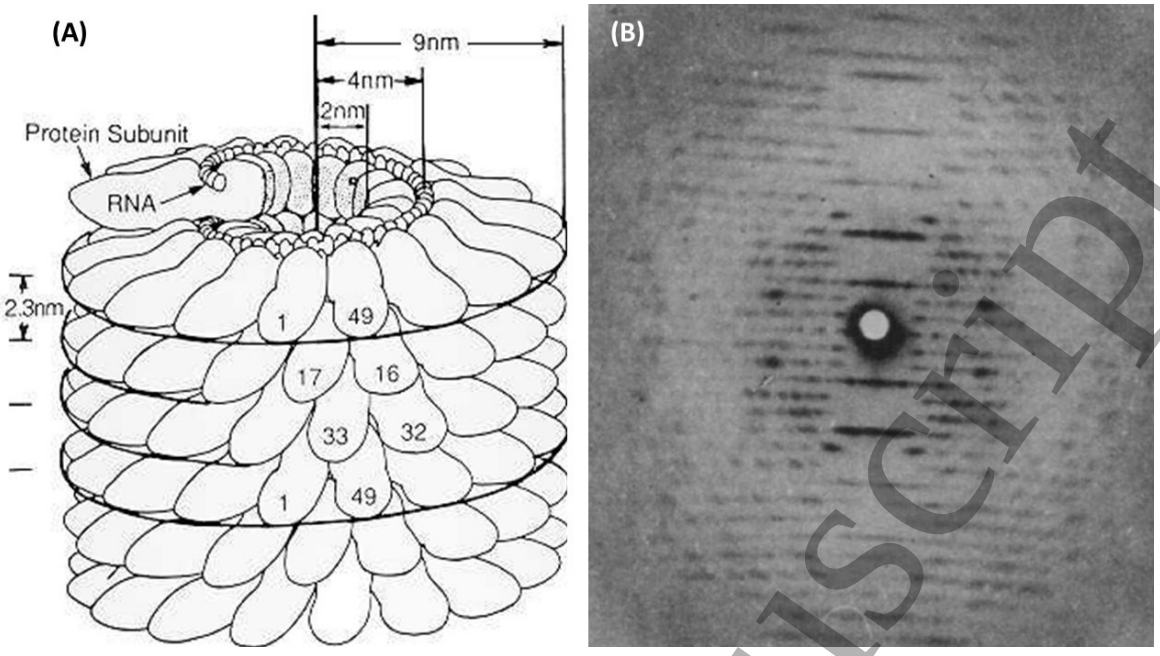

FIG. 14: (A) Diagram displaying the overall structure of TMV, which displays a rod-like appearance, 300 nm in length and 18 nm in diameter with a distinct inner channel of radius 2 nm. The protein scales whirl arond the helix axis with a repeat of 6.9 nm (49 subunits per three turns). Each turn contains a nonintegral number of subunits (16 plus 1/3), producing a pitch of 2.3 nm. About 5 percent of the length of a complete particle is shown [115]. (Reprinted from Advances in Protein Chemistry, 18, Caspar DLD, Assembly and Stability of the Tobacco Mosaic Virus Particle, 37-121, Copyright 1964, with permission from Elsevier.) (B) X-ray diffraction diagram of an orientated gel of Hg-substituted TMV common strain obtained by R. Franklin. The virus particles have their axes in the vertical direction. The horizontal layer-lines stratification corresponds to the axial repeat period of 6.9 nm [116]. (Reprinted by permission from Springer Nature, Rosalind E. Franklin, Structure of Tobacco Mosaic Virus, Nature, 175, 379 -381. Copyright 1955).

A. The Franklin-Caspar helical model

> *Her beautiful X-ray photographs fascinated me , and I was also able to interpret some that had apparently anomalous curved layer lines in terms of the splitting that occurs when the helical parameters are nonrational* (Aaron Klug commenting on Fig.14B) [22].

Since the presence of scale invariance symmetry is essential to QC structures, and spiral

patterns properly exhibit such a symmetry, in the quest for aperiodic crystals in biology it seems natural to start by considering structures combining circular shapes in a plane with translation symmetry along the perpedicular direction, thereby leading to the generation of conical helical curves in 3D. Indeed, helical based designs are ubiquous is structural biology, and they appear at different hierarchical levels ranging from the α-helix of proteins (Figs.3-4) and the DNA double-helix (Fig.11) macromolecular scales, to chromatin DNA supercoiling (Fig.5), and the TMV helical architecture (Fig.14) at supramamolecular scales.

From a chemical perspective, TMV is a relatively simple virus consisting of a single strand RNA molecule, adopting a hairpin loop structure 6390 bases long, coated with a single type of protein molecule only. Each protein monomer consists of 158 amino acids which are assembled into four main α-helices to bouild up the protein scales in the virus capsid. Notwithstanding this, the obtained fiber-diffraction diagrams were more complicated than those of DNA (Fig.11B), and it was not a simple task to index the large number of reflections. Fortunately, a number of certain unusual features in the X-ray diagram (referred to as layer-line splitting) could only be accounted for in terms of a helical design, involving a regular array of 2130 molecules of protein subunits around the RNA molecule, which is embedded at a radius of 4 nm offset from the helical axis (Fig.14A). The coat proteins self-assemble spiraling the RNA molecule, thereby defining a phyllotactic pattern similar to that observed in pineapples at a macroscopic scale, with three nucleotides residues per protein subunit, yielding 49 nucleotides and 16 1/3 proteins per helix turn [117]. Noteworthy, it was reported that the number of proteins per three turns of the helix is not exactly integral, and that this departure from an integer varied slightly among different strains of the virus. This effect is however very small and corresponds to a difference of only 1 to 3 proteins in the 2130 contained in the virus particle as a whole [117, 118].

B. The Caspar-Klug icosahedral model

The main structural problem in the study of virus exhibiting icosahedral protein shells can be stated as follows: How to construct a regular protein array with icosahedral symmetry formed by multiple copies of (nearly) identical chiral proteins interacting among them in (nearly) identical environments? If just one kind of chemical interaction would occur between each pair of interacting protein subunits, then arranging identical units in identical

environments would necessarily produce a symmetrical structure, and there would be only a geometrically limited number of kinds of symmetry available. In particular, icosahedral symmetry demands that the maximum number of asymmetric protein subunits that can be arranged on a surface with spherical topology, such that each has exactly the same environment, be 60 (Fig.15A). This is so because the chiral nature of proteins and their related capsomers imply the absence of both inversion and mirror symmetry elements in the resulting icosahedral virus capsid, hence halving the number of the icosahedral group symmetry elements from 120 (I_h group) to 60 (I group). Nevertheless, construction of icosahedral capsids containing just 60 protein subunits severely restricts the size of the genome that can be packaged inside, and it soon became evident that most viruses have considerably more than 60 protein subunits in their capsids. This fact provides a nice illustration of the balance between the amount of required biological information and geometrical size in biological systems [119]. Therefore, we must face the problem of how to form a closed shell exhibiting icosahedral symmetry using more than 60 protein subunits.

In this regard, the presence of different chemical *interaction centers* in the complex structure of a folded protein provides the basis for a straightforward matematization of such a protein in terms of suitable geometrical entities, where these *chemical centers* play the role of geometrical *points*. In this way, proteins exhibiting two different interaction centers may be assimilated to segments, those having three interaction centers to triangles (not necessarily equilateral), and so on. In fact, in order to account for most morphological units reported from microscopic imaging of virus particles one must assume the existence of at least *three* kinds of chemical interactions among neighboring proteins subunits involving three different interactions centers, which are generically referred to as *tail* (t), *head* (h) and *back* (b) ones (Fig.15B). These interactions are related to a specific symmetry element of the icosahedral group, namely:

- $h-h$ interactions, involving two proteins in front of each other (related to 2-fold axis),
- $b-b-b$ interactions, involving three proteins in a triangular configuration (related to 3-fold axis), and
- $t-t-t-t-t$ interactions, involving five proteins in a pentagonal arrangement (related to 5-fold axis).

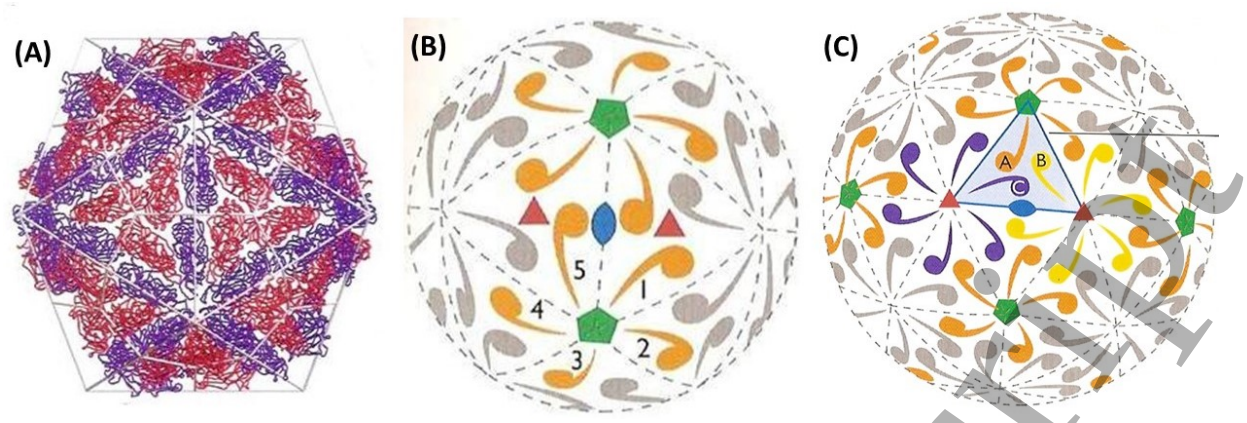

FIG. 15: A) The capsid of the L-A virus particle (viewed down to an icosahedral 2-fold axis) is made of 60 protein subunit dimers grouped in capsomers containing five dimers each [120]. (Adapted by permission from Springer Nature, Nature Structural Biology, L-A virus at 3.4 $\AA$ resolution reveals particle architecture and mRNA decapping mechanism, Naitow H, Tang J, Canady M, Wickner R B, Johnson J E, 9 725-728. Copyright 2002). B) Sketch showing an ideal icosahedral packing in simple icosahedral virus structures with triangulation number $T = 1$. A comma represents a single protein chiral molecule which forms the basic structural unit by itself, and every molecule is related to its neighbors through head-to-head, back-to-back and tail-to-tail interactions, respectively corresponding to the 2-fold, 3-fold and 5-fold axes characteristic of icosahedral symmetry. C) In the $T = 3$ structure, able to accommodate 180 proteins, there are three modes of packing protein subunits to obtain the basic structural unit. The A units are present in pentamers, formed by tail-to-tail interactions. The B and C subunits are arranged in rings of six molecules via tail-to-tail interactions as well (Adapted from [121]).

Note that no $t - b$, $h - t$ or $h - b$ interactions are allowed to occur. Furthermore, it is assumed that, although tail, back and head interactions involve different protein locations, all of them exhibit the *same* intensity and directional properties (i.e., they are effectively isotropic). These are the main tenets of the so-called *quasi-equivalence principle* (QEP), originally introduced in 1962 by Donald L. D. Caspar and Aaron Klug on the basis that the lowest energy capsid structure is expected to have the maximum number of most stable chemical interactions formed [122]. According to the QEP, protein subunits can be positioned on a *triangulated* icosahedral surface lattice such that the environments of the individual proteins could be similar although not identical. The size of the capsid shell can

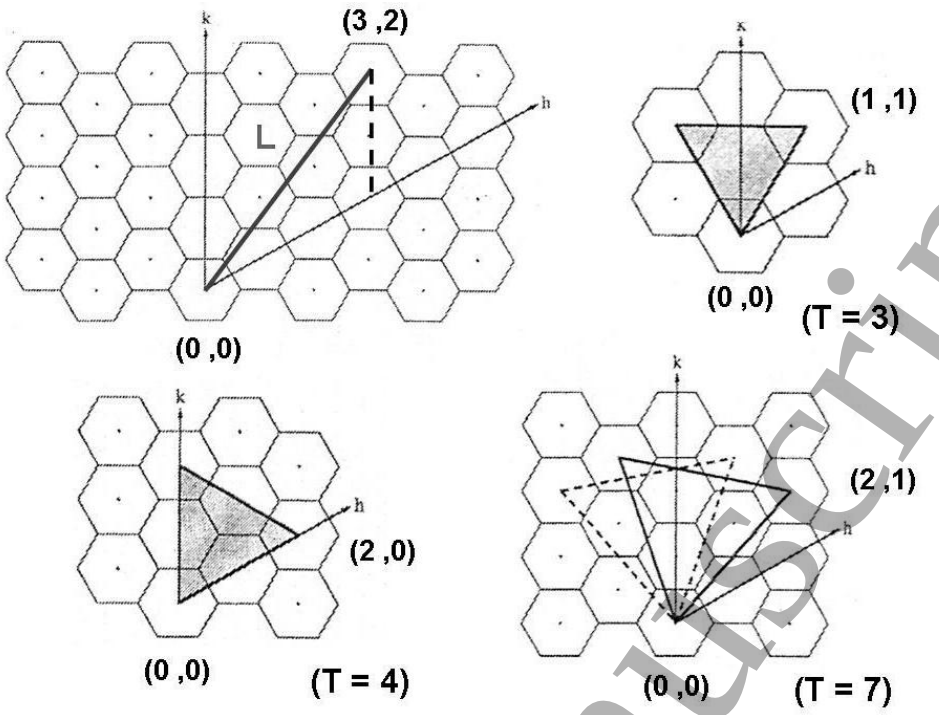

FIG. 16: Geometric procedure for generating Goldberg polyhedra with different triangulation numbers from a hexagonal planar lattice. The vertices of regular triangular faces of the Goldberg polyhedron hexagons coincide with the 6-fold axes of the plane hexagonal lattice. The coordinates of the hexagons centers are referred to the axes **h** and **k**.

then be properly increased, still preserving the basic icosahedral design shown in Fig.15B, by partitioning the surface of this icosahedron into a larger number of triangles, which are subsequently properly scaled up (Fig.15C). But now the facet triangles will no longer all have the protein subunits located in equivalent positions, so that the three protein subunits originally assigned to each triangular face will not generally occupy equivalent environments. In particular, the presence of hexagonal rings containing six protein subunits, which apparently are not compatible with icosahedral symmetry, naturally occur. In this way, the resulting polyhedra will be able to accommodate $12 \times 5 + 10(T-1) \times 6 = 60T$ protein subunits, where T is the so-called triangulation number. Accordingly, the assembly of viral capsids exhibiting six 5-fold, ten 3-fold and fifteen 2-fold icosahedral symmetry axes can be physically realized, albeit containing *local* hexagonal patterns as well.

Remarkably enough, the problem of arranging units in a hexagonal close packing on

an icosahedral surface, with local pentagonal arrangements at certain vertices, had earlier been solved by Michael Goldberg in 1937, who introduced a type of polyhedra particularly well suited to this end [123]. Indeed, the so-called Goldberg polyhedra are convex polyhedra defined by the following properties: (1) each face is either a hexagon or pentagon, (2) exactly three faces meet at each vertex, and (3) they have full rotational icosahedral symmetry (I group). Icosahedral symmetry ensures that the pentagons must be regular ones, although many of the hexagons may not be. Goldberg polyhedra can be derived from a hexagonal plane periodic lattice by converting some of the hexagons to pentagons. Once an origin is defined, every hexagon in the lattice can be uniquely identified by the number of steps along the **h** and **k** directions in the hexagonal net (Fig. 16). To construct a given Goldberg polyhedron, one face of the desired scaled up polyhedron is drawn in the hexagonal net. The origin is replaced with a pentagon, as well as the hexagon located at the (h, k) position. The third replaced hexagon is then obtained by completing an equilateral triangle. These substitutions have the effect of folding the plane into a closed surface. To this end, since an icosahedron has 6 axes with 5-fold symmetry, twelve pentagons must be introduced in the lattice in substitution to hexagons to form a closed structure with icosahedral symmetry. In the simplest case, all the hexagons around a given origin are converted to pentagons and a pentagonal dodecahedron in obtained. Therefore this Platonic solid is but a particular case of the more general family formed by Goldberg polyhedra.

In the more general cases the locations of the substituted pentagons are given by the so-called Goldberg indices (h, k), where $h, k \in \mathbb{N}$, are the indices of the hexagonal translation mapped onto the edge. In this way, the triangulation number naturally appears in the process of obtaining a Goldberg polyhedron from a hexagonal net, and it is given by the ratio between the area of the polyhedron equilateral triangle face of size L on the hexagonal lattice and the area of a reference equilateral triangle of size $L_0 = 1$, that is (see Fig.16)

$$T = \frac{\frac{\sqrt{3}}{4}L^2}{\frac{\sqrt{3}}{4}} = L^2 = h^2 + k^2 - 2hk\cos\frac{2\pi}{3} = h^2 + k^2 + hk. \tag{17}$$

This number then gives the number of facets per face. We note that T is invariant under the exchange $h \leftrightarrow k$. The significance of this number is that it introduces a selection rule, so that only certain numbers of protein subunits are able to form closed polyhedral shells. In fact, since an icosahedron has 20 faces, and each facet is assumed to have three protein subunits, one gets $60T$ protein subunits in total in a virus capsid characterized

by a given T number. Therefore, this number allows for a systematic classification of the virus capsids arranged according to the (h, k) indices. In this way, the T number provides a measure of the structural complexity of viruses capsids. In the simplest $T = 1$ case $(h = 0, k = 1)$ the interactions of all protein subunits with their neighbors are identical, leading to a pentagonal dodecahedron overall arrangement of the capsid shell. Two main capsid geometries have been reported for the next structure in complexity degree ($T = 3$). The most common is a truncated icosahedron (an Arquimedean solid), which exhibits the basic arrangement of 12 vertices with 5-fold symmetry clusters along with 20 hexagonal facets interposed between them. On the other hand, there also exist $T = 3$ class virus capsids (e. g., nonadavirus, tomato bushy stunt virus, bean mosaic virus) which *cannot* be described in terms of Goldberg polyhedra, since they lack hexagonal facets. Indeed, in this case the capsid shape is described by a rhombic triacontahedron, which is a Catalan solid comprising 30 golden rhombi forming a dihedral angle of $2\pi/5$, which are joined at 60 edges and 32 vertices, of which twelve are 5-fold and twenty are 3-fold ones (see Fig.6D). Accordingly, the $T = 3$ capsids exhibiting a rhombic triacontahedron shape are structurally simpler than truncated icosahedron ones, since they lack hexagonal arrangements but low symmetry rhombic ones, and we only require one type of geometrical motive (golden rhombi) instead of the pentagons and hexagons present in truncated icosahedra. Quite interestingly, the rhombic triacontahedron plays a very important role in the structural design of an important class of intermetallic QCs belonging to the so-called Tsai-type class [124].

C. Quasi-equivalence principle shortcomings

During the 1980s several viruses with relatively large T values were observed to show some features not compatible with the standard Caspar and Klug model and a growing number of virus capsids structures not satisfying this model tenets have been reported since then. A representative example is provided by papovaviruses, which are oncogenic viruses that include the polyoma and papilloma virus subfamilies. The papovaviruses have a common capsid structure composed of 72 capsomers, and they were early classified as belonging to the $T = 7d$ class on the basis of low-resolution micrographs [125], thereby implying their capsids were made of 420 protein subunits. Later on, the structure of polyoma virus was determined at a higher resolution by single crystal X-ray diffraction in 1982, and the 5-fold

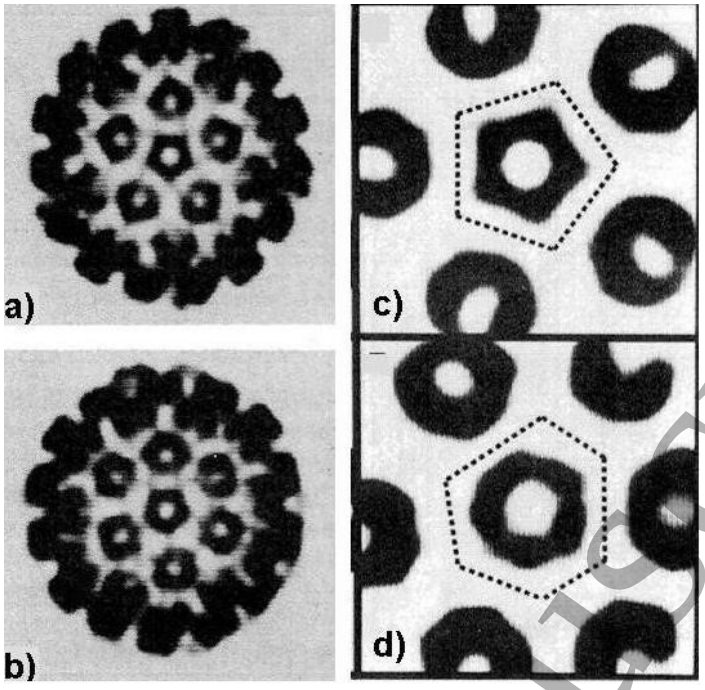

FIG. 17: Electron microscopic views of half the capsid of bovine papilloma virus (about 60 nm in diameter) down the 5-fold a) and 6-fold b) axes. Electron density sections showing the substructure of the pentavalent c) and hexavalent d) morphological units indicate they are pentamers formed by five interacting proteins in both cases [126]. (Reprinted by permission from Springer Nature, Nature (London) 295 110-115, Polyoma virus capsid structure at 22.5 $\AA$ resolution, Rayment I, Baker T S, Caspar D L D, and Murakami W T, Copyright 1982).

symmetry present in the diffraction data was interpreted as indicating that *all* 72 capsomers present on the virus surface were built from five identical or very similar protein *pentamers* coordinated to their neighbors in *both* hexavalent and pentavalent configurations (Fig.17) [126]. Thus, in these virus capsids, there exist 12 *pentavalent* pentamers making edge-to-edge contacts with their neighbors and 60 *hexavalent* pentamers, instead of 12 pentamers and $10(T-1)$ hexamers as expected on the basis of the Caspar-Klug model. Then, the capsids of papovaviruses actually contain $12 \times 5 + 60 \times 5 = 360$ protein subunits, which would correspond to a hypothetical $T = 6$ value that is not really allowed by the triangulation number selection rule given by Eq.(17). Therefore, the notion of hexamer and pentamer capsomers must be replaced in this case with that of hexavalent (respectively pentavalent) capsomers instead. On the other hand, the capsid of dengue virus and the capsids of other

flaviviridae (Zika virus, yellow fever virus, western Nile virus) do not contain hexamers at all. Likewise, the capsids of large viruses of asfarviridae, ascoviridae, iridoviridae, poxviridae, mimiviridae, and phycodnaviridae viral families do not contain any hexamers either, but instead have trimers and pentamers as their structural units. Therefore, the assumption of QEP is too restrictive for many viruses.

This drawback has spurred alternative approaches, which consider the entire virus capsid as an extended chemical network involving local protein interaction centers located at specific amino acid residues as playing the role of effective *chemical lattice* points. On the basis of these chemical points (vertices) one may introduce segments (edges), planes (polygonal tiles) and polyhedra in order to describe the modular design characteristic of virus capsids. In this way, the hexagonal lattice picture in terms of triangulations is no longer necessary, permitting tesselations in terms of other shapes, such as rhombi, trapezoids, or pentagons. Due to the requirement of 5-fold symmetry axis, some of these tiles need to have some corner with an angle of $2\pi/5$. These criteria then represent a generalization of the QEP in the context of a tiling approach [127]. In accordance with this generalized QEP, protein subunits (represented by dots) must be located at those corners of the tiles which subtend the same angle, thereby ensuring that identical types of protein subunits can only occupy structurally equivalent sites on the tiles. This generalization naturally translates as certain requirements on the *decoration* of the tiles. As we see, the proposed tiles have more vertices where the different protein subunits may be allocated than in the triangular tiles case, so that certain criteria must be adopted in order to properly assign which vertices are related to a protein subunit and which ones are not. To this end, the knowledge gained from aperiodic tilings can be fruitfully used. Since pentagons can not tessellate the plane without gap nor overlaps, a straightforward extension of the Goldberg construction is not possible. The use of aperiodic tiling notions, originally introduced in the study of quasicrystalline alloys, has been successfully borrowed to properly classify the protein structure of certain virus families during the last decade. Thus, the possible design of suitable generalized lattices via projection from higher-dimensional lattices with icosahedral symmetry was studied in detail [128]. On the other hand, it was demonstrated that the location of different protein subunits on the virus capsid can be precisely determined by properly blending rotational and invariance scale symmetries in a 6D crystallographical space, thereby introducing an elegant unified approach entirely based on mathematical notions borrowed from the QCs

science toolkit. In this case, the Seitz symbol reads

$$\mathbf{W_V s} = \begin{pmatrix} \mathbf{R} & \mu\mathbf{t} \\ \mathbf{0} & 1 \end{pmatrix} \mathbf{s}, \tag{18}$$

where $\mathbf{R}$ describes a rotation operator in the 6D hyperspace, vectors $\mathbf{t}$ and $\mathbf{0}$ have six components each, and $\mathbf{s} = (x_1, x_2, x_3, x_4, x_5, x_6, 1)^T$ [129, 130].

D. Virus quasicrystals?

> "*But with Ammann's non-periodic solids as basic units, one would arrive at quasiperiodic 'crystals' involving such seemingly impossible (crystallographically) cleavage directions along dodecahedral or icosahedral planes. Is it possible that the viruses might grow in some such a way involving non-periodic basic units – or is the idea too fanciful?*" (Roger Penrose to Martin Gardner, letter dated on May 4, 1976) [131].

In Table I we list the crystallographical data of different virus crystal representatives, including all possible classical crystallographical systems. It is interesting to note that, depending upon the adopted growth conditions certain virus can crystallize in different systems. For instance, GFLV virus crystals corresponding to spatial groups P1 (1, triclinic), P2 (3, monoclinic) and $P2_13$ (198, cubic) have been reported [138].

Virus crystallization is ruled by a combination of chemical and geometrical factors, where the size and relative orientation of the capsids along the resulting crystal symmetry axes play a fundamental role. In this regard, it was a fortunate fact that all TBSV virus particles will adopt the same spatial configuration in the final crystalline array, hence providing X-ray diffraction patterns amenable to be easily interpreted. This virus crystallizes into a fcc lattice (spatial group I23), so that two symmetry axes of the virus capsid are oriented along crystal directions, namely, a 2-fold axis along [100] and a 3-fold axis along the [111] directions, respectively, so that the capsid's 5-fold symmetry axis are effaced from the resulting virus crystal. On the contrary, in TYMV virus crystals the capsids lie with their centres at the lattice points of a bcc unit cell of side 35 nm, but are not all of them in the same orientation, so that the true crystallographic unit cell has a side of 70 nm (8 times larger than that of TBSV) and contains 16 virus particles within [117].

Chemical aspects play a key role when different viruses crystallize into similar growth habits. This is the case, for instance, of poliovirus and rhinovirus (both members of the picornavirus family) isomorphic crystals (see Table I), depending on a precise correlation among the chemical interaction centers of all the involved capsids [134]. Detailed studies aimed at evaluating the balance between chemical and purely geometrical factors in the resulting growth habit of virus crystals, have disclosed that the relative size of capsids along with their different symmetry axes play a significant role in the emergence of local ordering effects in global low-symmetry crystals, such as those belonging to monoclinic and triclinic systems [132].

As we discussed in Sec.IV A, there is no structural reason why a helix should contain an exact integral ratio of subunits to turns, and the 49/3 ratio value obtained in the TMV case is merely the nearest rational approximation to the number of protein subunits in three helix turns [117]. Consequently, the capsid proteins distribution in TMV could be properly regarded as an aperiodic structure itself, so that the crystals resulting from their condensation may be reasonably considered to be aperiodic crystals candidates as well. In the same vein, is it possible that an ensemble of icosahedral virus particles may eventually pile up to give rise to a full-fledged icosahedral virus QC? To the best of my knowledge the existence of such a sort of soft matter biological QC has not yet been reported, and its search would be a very interesting quest for the time to come.

V. OUTLOOK AND PERSPECTIVES

Is there a specific scale range for life processes to preferentially occur? Attending to the available information significant processes of biological importance have been reported encompassing molecular, macromolecular, supramolecular, subcellular, cellular, or multicellular scales in a nested way. In Sec.I we learnt that most biological hierarchical designs are not strictly fractal, because some new structures progressively emerge as we zoom out the viewpoint ranging from smaller to larger spatial scales. Accordingly, rigorous self-similar symmetry only applies within restricted spatial domains. This feature reflects the difference between growing by successive assembling of different sorts of building blocks, as it occurs in the workings of life, versus a systematic yuxtaposition of a given motif throughout the space, either periodically or aperiodically, as is the case in non-living growth processes. Therefore,

albeit all fractal structures obey a hierarchical design, most hierarchical structures observed in biological systems can not be properly described in terms of rigorous geometrical fractals, and they go far beyond them in both complexity and design richness.

In biological systems the emergence of distinct structures at different scales stems from the presence of different kinds of interactions, such as covalent or hydrogen bondings, van der Waals, dipole, ionic, hydrophobic/hydrophilic or steric forces among the involved building blocks, whose relative importance alternates depending on the considered scale range, hence naturally resulting in a regurlarly clustered growth. This progressive unfolding, ruled by the above mentioned physico-chemical interactions, also favors the predominance of certain symmetrical designs, such as helical and icosahedral shapes at macromolecular and supramolecular scales, or polygonal and polyhedral shapes at the cellular/tissues domains. Accordingly, pathological states can appear in living beings at anyone of their characteristic structural scales, stemming from either symmetry breaking effects or/and anomalous crystallization/condensation processes. For instance, amyloidosis related deseases, such as Alzheimer, Parkinson, or Creutzfeldt-Jacob disorders, share a common etiology closely related to the formation of plaques resulting from polypeptide fibrous-like assemblies in the brain tissue [139, 140]. In a similar vein, to gain a deeper undertanding on the way certain living organisms synthesize the specialized mineralized structures they contain, as well as to identify the organic molecules and physico-chemical processes that control the resulting spatial arrangements determining their unique physical properties, is highly relevant for medical applications. This knowledge also provides a source of inspiration for the design of advanced biomaterials, such as synthetic calcium phosphates. These versatile biomaterial chemically resemble the inorganic phase present in hard tissues (e.g., bone, dentine, fish scales, or horns of different animals) as well as pathological calcifications (e.g., dental and urinary calculi, tendon mineralization, calcification of blood vessels). Therefore, the synthesis of calcium phosphates under physiological conditions, mediated by organic additives resembling the small molecules or large macromolecules of the organic matrix of bones and teeth, is a matter of intensive research nowadays [141, 142]. To the best of my knowledge no aperiodic crystal structures have been reported in the study of such a biomineralization processes to date, and it would be interesting to further explore such a possibility.

Through Secs.II-IV we have seen that in many instances the currently adopted QC notion is not general enough to properly account for the rich structural features one usually finds

in biological arrangements of matter. Notwithstanding this, the knowledge gained from the study of QCs thus far provides a very convenient modeling framework to start with in many instances. In this regard, the following analogies between biological patterns and aperiodic crystal designs are worth to be highlighted:

- Global scale invariance symmetry is present in both QCs and spiral based phyllotactic patterns.

- The cut-and-project method can be used in the description of both metallic QCs, soft-matter based QCs and phyllotactic patterns. In particular, dislocation dipoles are organized along circles related to 1D *circular* quasicrystals (see Fig.12B).

- The recourse to higher dimensional spaces can be fruitfully exploited to describe aperiodic crystals (including QCs) as well as several biological systems, such as sea urchins (e. g., via the eutectic star formalism). In this way, a mathematical tool which had been previously introduced to describe transformations from quasiperiodic to periodic tilings via rotations taking place in a higher dimensional space [143, 144], proved extremely useful for studying biological issues as well.

- Aperiodic tilings early used in the description of atomic distributions in quasicrystalline metallic alloys can be extended to describe the arrangement of proteins in virus capsids. In this way, new approaches to virus structural analysis have been introduced, providing a viral tiling theory which describes the locations of the proteins subunits and their bonds on the basis of mathematical tools derived from the study of QCs structure.

In summary, we realize that condensed matter structures usually found in biological systems display beautifully functional complex patterns whose detailed geometrical description strongly suggests the convenience of introducing concepts extending beyond both periodic and quasiperiodic crystal notions. This goal nicely fits within the grand conceptual framework early dubbed *generalized crystallography* by Alan L. Mackay [145–148], who laid down the expansion of crystallography by emphasizing the importance of self-similarity, hierarchy, and information, as well as the convenience of higher dimensional and non-Euclidean approaches to develop a unified way of dealing with a broad collection of spatial structures and

their changes, growth, evolution and transformations. In this context, the very notion of *hypercrystal* may be regarded as a step forward towards a broader crystal notion, naturally encompassing both periodic and aperiodic crystals alike, in order to conceptually unify all the disciplines in which crystals play a significant role, not only in mineralogy, solid state physics, structural chemistry and material sciences, but also in biochemistry, molecular biology, genetics, virology, or medicine. A unification in which the general mathematical notion of almost periodic functions, heralded by Harald Bohr long time ago [149], will probably play a useful guide [150].

Acknowledgements

I warmly thank M. Victoria Hernández for a critical reading of the manuscript.

[1] J A Adam, *Mathematics in Nature – Modeling Patterns in the Natural World* (Princeton University Press, Princeton, 2003).

[2] J D Bernal, The scale of structural units in biopoesis, in *Aspects of the Origin of Life*, M. Florkin (ed.) (Pergamon Press, Oxford, 1960) pp.155-169.

[3] J H E Cartwright, A L Mackay, Beyond crystals: the dialectic of materials and information, 2012 Phil. Trans. R. Soc. A **370**, 2807-2822.

[4] B Mandelbrot, *The Fractal Geometry of Nature* (W H Freeman & Co., New York, 1982).

[5] E A Lord, A L Mackay, S Ranganathan, *New Geometries for New Materials* (Cambridge University Press, Cambridge, 2006).

[6] A McPherson, L DeLucas, Microgravity protein crystallization, 2015, Microgravity **1** 15010, doi: 10.1038/npjmgrav.2015.10.

[7] T Goddard, http://www.rbvi.ucsf.edu/Research/afm/stmv/afmaverage.html .

[8] http://viperdb.scripps.edu/.

[9] V V Isaeva, N V Kasyanov, Symmetry transformations in metazoan evolution and development, 2021 Symmetry **13**, 160. https://doi.org/10.3390/sym13020160.

[10] S Koszelak, J Day, C Leja, R Cudney, A McPherson, Protein and virus crystal growth on International Microgravity Laboratory-2, 1995 Biophys. J **69**, 13-19.

[11] J H E Cartwright, A G Checa, The dynamics of nacre self-assembly, 2007 J. R. Soc. Interface **4**, 491-504.

[12] N Reznikov, M Bilton, L Lari, M M Stevens, R Kroger, Fractal-like hierarchical organization of bone begins at the nanoscale, 2018 Science **360**, eaao2189.

[13] M Georgiadis, R Muller, P Schneider, Techniques to assess bone ultrastructure organization: orientation and arrangement of mineralized collagen fibrils, 2016 J. R. Soc. Interface 13: 20160088. http://dx.doi.org/10.1098/rsif.2016.0088.

[14] A H Zewail, Physical biology – 4D visualization of complexity, in *Physical Biology: From Atoms to Medicine* A H Zewail (ed.) (Imperial College Press, London, 2008) pp.23-49.

[15] Collagen is the main structural protein in the extracellular matrix found in connective tissues, such as cartilage, bones, tendons, ligaments, and skin, making up from 25% to 35% of the whole-body protein content.

[16] Keratin represents the most abundant structural protein of hair, nails, horn, hoofs, wool, feathers, as well as of the epithelial cells in the outermost layers of the skin and, together with collagen, is the most important biopolymer in most animals.

[17] The secondary structure of proteins expresses the geometry of their polypeptide chains and it results from various interaction forces, including peptide bond, hydrogen bonds, and steric repulsion between amino acids side groups.

[18] B Wang, W Yang, J McKittrick, M A Meyers, Keratin: Structure, mechanical properties, occurrence in biological organisms, and efforts at bioinspiration, 2016 Progress in Materials Science, **76**, 229-318.

[19] K Lin, D Zhang, M H Macedo, W Cui, B Sarmento, G Shen, Advanced Collagen Based Biomaterials for Regenerative Biomedicine 2019, Adv. Functional Mats., **29**, 1804943, https://doi-org.bucm.idm.oclc.org/10.1002/adfm.201804943.

[20] M Hadian, B M Corcoran, R I Han, J Gunter Grossmann, J P Bradshaw, Collagen organization in canine myxomatous mitral valve disease: An X-Ray diffraction study, 2007 Biophys. J., **93**, 2472-2476.

[21] https://www.oist.jp/news-center/photos/diagram-chromatin-nucleosome-structure

[22] A Klug, From virus structure to chromatin: X-ray diffraction to three-dimensional electron microscopy, 2010 Annu. Rev. Biochem. **79**, 1-35.

[23] F Michor, J Liphardt, M Ferrari, J Widom, What does physics have to do with cancer? 2011,

Nature Rev. Cancer **11**, 657-670.

[24] Photo by Aaron Burden on Unsplash (https://unsplash.com/photos/OfVNh6YCJ6o).

[25] Photo by Hermann Schachner (https://commons.wikimedia.org/w/index.php?curid=29910109/).

[26] Each ommatidium contains a cluster of photoreceptor cells surrounded by support cells and pigment cells. The outer part of the ommatidium is overlaid with a transparent cornea. A hexagonal lattice of pigment cells insulates the ommatidial core from neighboring ommatidia to optimize coverage of the visual field, which therefore affects the acuity of animal's vision.

[27] T A Cook, *The Curves of Life* 1914 (Reprinted. Dover Press, New York, 1979).

[28] I Adler I, D Barabé, R V Jean, A history of the study of phyllotaxis, 1997 Ann. Bot. **80** 231-244.

[29] B Razin, *Double Helix of Phyllotaxis – Analysis of the Geometric Model of Plant Morphogenesis* (Brown Walker Press, Boca Raton, 2020).

[30] D C Winfield, K M Harris, Phyllotaxis-based simple patterns, 2001 Patent number WO 01/26749 A1.

[31] A González, Measurement of areas on a sphere using Fibonacci and latitude-longitude lattices, 2010 Math. Geosci. **42**, 49-64

[32] C Kuhlemeier, Phyllotaxis, 2007 Trends Plant Sci. **12**, 143-150.

[33] R Jean, *Phyllotaxis. A Systematic Study in Plant Morphogenesis* (Cambridge University Press, Cambridge, 1994).

[34] C Golé, J Dumais, S. Douady, Fibonacci or quasi-symmetric phyllotaxis. Part I: why? 2016, Acta Soc. Bot. Pol. **85**, 3533.

[35] D Barabé, Stochastic approaches in phyllotaxis, 2006 Can. J. Bot. **84**, 1675-1685.

[36] H S M Coxeter, *Introduction to Geometry* (John Wiley & Sons, New York, 1961), Chapter 11.

[37] K Yalta, S Ozturk, E Yetkin, Golden ratio and the heart: A review of divine aesthetics, 2016 Int. J. Cardiol. **214**, 107-112.

[38] L Bravais, A Bravais, 1837 Ann. Sci. Nat. second series **7**, 42-110, 198-221, and 291-348; **8**, 11-42; 1839 Essai sur la disposition générale des feuilles, **12**, 5-14 and 65-77.

[39] A Bravais, Memorie sur les systèmes formé par des points distribués régulèrmient sur un plan ou dans l'espace, J. Ec. Polytech. 1850 **19**, 1-128.

[40] Jean R V *Mathematical approach to Patterns and Form in Plant Growth* (Wiley, New York, 1984),

[41] G J Mitchison, Phyllotaxis and the Fibonacci series, 1977 Science **196** 270-275.

[42] M Livio, *The Golden Ratio* (Broadway Books, New York, 2002).

[43] M Naylor, Golden, $\sqrt{2}$, and π flowers: A spiral story, 2002 Math. Mag. **75**, 163-172.

[44] S Strogatz, *Infinite Powers – How Calculus Reveals the Secrests of the Universe* (Eamon Dolan Book, Boston, 2019).

[45] N Rivier, R Occelli, J Pantaloni, A Lissowski, Structure of Benard convection cells, phyllotaxis and crystallography in cylindrical symmetry, 1984 J. Phys. France **45** 49-63.

[46] L A Bursill, P J Lin, F Xudong, Spiral lattice concepts, 1987 Mod. Phys. Lett. B **1** 195-206.

[47] H Vogel, A better way to construct the sunflower head, 1979 Math. Biosci. **44** 179-189.

[48] N Rivier, J-F Sadoc, J Charvolin, Phyllotaxis: a framework for foam topological evolution, 2016 Eur. J. Phys. E **39**, 7.

[49] F Xudong, L A Bursill, P J Lin, Fourier transforms and structural analysis of spiral lattices, 1988 Int. J. Mod. Phys. B **2** 131-146.

[50] E. Maciá-Barber, *Aperiodic Structures in Condensed Matter* (CRC Taylor & Francis, Boca Raton, 2009).

[51] We can carry out the transformation from a given Cartesian coordinate system to another by means of three successive rotations performed in a specific sequence. For instance, in the study of the rigid-body dynamics the so-called Euler angles given by θ (nutation), ϕ (precession), ψ (spin) are profusely used. For Eulerian angles, the rotation is about the Z-axis (producing rotated X,Y axes, usually designated as X' and Y'), followed by rotation about the X' axis (producing Y" and Z" axes) and finally followed by a rotation about the Z" axis, which is given by the product $\mathbf{R} = \mathbf{R}_{Z''}(\psi)\mathbf{R}_{X'}(\theta)\mathbf{R}_{Z}(\phi)$. See, for instance, L Meirovitch, *Methods of Analytical Dynamics* (McGraw-Hill. New York, 1970) pp.140-143.

[52] L Zeng, G Wang, Modeling golden section plants, 2009 Prog. Nat. Sci. **19**, 255-260.

[53] M de Graef, M E McHenry, *Structure of Materials – An Introduction to Crystalography, Diffraction and Symmetry* (2nd. ed, Cambridge University Press, Cambridge, 2012).

[54] To this end, the components of both matrix $\mathbf{D}$ and vector $\mathbf{t}$ must be referred to a common basis.

[55] M Torres, G Pastor, I Jiménez, F Montero de Espinosa, Five-fold quasicrystal-like germinal

pattern in the Faraday wave experiment, 1995 Chaos Solitons & Fractals **5**, 2089-2093.

[56] H S M Coxeter, *Regular Polytopes* (Dover, New York, 1973).

[57] C Contreras-Figueroa, L Hernández-Sandoval, J L Aragón, A measure of regualrity for polygonal mosaics in biological systems, Theor. Biol. Med. Model. 2015, **12**, 27.

[58] H Hadwiger, Hüber ausgezeichnete vektorsterne unr reguläre polytope, 1940 Comentarii Matematici Helvetic 13, 90-108.

[59] J L Aragón, A Gómez-Rodríguez, M Torres, Simplified dynamic model for motility of irregular echinoids, 2005 Phys. Rev. E **72**, 041925.

[60] M Torres, J L Aragón, P Domínguez, D Gil, Regularity in irregular echinoids, 2002 J. Math. Biol. **44**, 330-340.

[61] J López-Sauceda, J L Aragón, Eutacticity in sea urchin evolution, 2008 Bull. Math. Bio. **70**, 625-634.

[62] B Christiansen, P Alstrom, M T Levinsen, Ordered capillary-wave states: Quasicrystals, hexagons, and radial waves, 1992 Phys. Rev. Lett. **68**, 2157-2160.

[63] J P Gollup, J S Langer, Pattern formation in nonequilibrium physics, 1999 Rev. Mod. Phys. **71**, S396-S403.

[64] R Lifshitz, D M Petrich, Theoretical model for Faraday waves with multiple-frequency forcing, 1997 Phys. Rev. Lett. **79**, 1261-1264.

[65] P Chen, J Viñals, Pattern selection in Faraday waves, 1997 Phys. Rev. Lett. **79**, 2670-2673.

[66] R A Barrio, J L Aragón, C Vera, M Torres, I Jiménez, F Montero de Espinosa, Robust symmetry patterns in the Farady experiment, 1997 Phys. Rev. E **56**, 4222-4230.

[67] J L Aragón, M Torres, D Gil, R A Barrio, P K Maini, Turing patterns with pentagonal symmetry, 2002 Phys. Rev. E **65**, 051913.

[68] L Costa, F Rocha, S Lima, Characterizing poligonality in biological structures, 2006 Phys. Rev. E **73**, 011913.

[69] Y Yamagishi and T Sushida, Archimedean Voronoi spiral tilings, 2018 J.Phys. A: Math. Theor. **51**, 045203.

[70] M Bock, A Kumar Tyagi, J-U Kreft, W Alt, Generalized Voronoi tessellation as a model of two-dimensional cell tissue dynamics, 2010 Bull. Math. Biol. **72**, 1696-1731.

[71] Y Yamagishi, T Sushida, J-F Sadoc, Area convergence of Voronoi cells on spiral lattices, 2021 Nonlinearity **34** 3163-3183.

[72] M Pisco, F Galeotti, Nano- and micropatterning on optical fibers by bottom-up approach: The importance of being ordered, 2021 Appl. Sci. **11**, 3254.

[73] J C Sadoc, N Rivier, J Charvolin, Phyllotaxis: a non-conventional crystalline solution to packing efficieny in situations with radial symmetry, 2012 Acta Cryst. **A68**, 470-483.

[74] Schrödinger E, *What is life? The Physical aspects of the Living Cell*, (Cambridge University Press, New York 1945).

[75] E Artacho, M Machado, D Sánchez-Portal, P Ordejón, J M Soler, Electrons in dry DNA from density functional calculations, 2003 Molecular Phys. **101**, 1587.

[76] E Maciá, Charge transfer in DNA: effective Hamiltonian approaches, Z. Kristallograph. 2009 **224** 91-95.

[77] E. Maciá, The role of aperiodic order in science and technology, 2006 Rep. Prog. Phys. **69**, 397-441.

[78] International Union of Crystallography Report of the Executive Committee for 1991 Acta Cryst. A **48** 922 (1992). See also https://www.iucr.org/iucr/commissions/aperiodic-crystals. Last accessed 4 March 2021.

[79] T Janssen, G Chapuis, and M de Boissieu, *Aperiodic Crystals: From Modulated Phases to Quasicrystals* (Oxford University Press, 2nd. Ed., Oxford, 2018).

[80] M de Boissieu, Ted Janssen and aperiodic crystals, 2019 Acta Cryst. A **75**, 273-280.

[81] E. Maciá-Barber, *Quasicrystals: Fundamentals and Applications* (CRC Taylor & Francis, Boca Raton, 2021).

[82] Shechtman D, Blech I, Gratias D, Cahn J W, Metallic phase with long-range orientational order and no translation symmetry, 1984 Phys. Rev. Lett. **53**, 1951-1954.

[83] A Schönleber, Organic molecular compounds with modulated crystal structure, 2011 Z. Kristallogr. **226**, 499-517.

[84] W Steurer, S Deloudi, *Crystallography of Quasicrystals - Concepts, Methods and Structures*, Springer Series in Materials Science 126 (Springer Verlag, Berlin, 2009).

[85] Levine D, Steinhardt P J, Quasicrystals: A new class of ordered structures, 1984 Phys. Rev. Lett. **53**, 2477-2480.

[86] Y Couder, S Douady, Phyllotaxis: the avoidance of rationals and a relation with quasi-crystals, in Proceedings of the 19th IUPAP International Conference on Statistical Physics (ed. B L Hao, 1996) 121-127.

[87] S van Smaalen, Modulated Crystal Structures. In *Handbook of Solid State Chemistry* (eds R. Dronskowski, S. Kikkawa and A. Stein, 2017). https://doi.org/10.1002/9783527691036.hsscvol3008

[88] A Janner, Which symmetry will an ideal quasicrystal admit? 1991 Acta Cryst. A **47** 577-590.

[89] A Janner, Towards a classification of icosahedral viruses in terms of indexed polyhedra, 2006 Acta Cryst. A **62** 319-330.

[90] J Smietanska, J Sliwiak, M Gilski, Z Dauter, R Strzalka, J Wolny, M Jaskolsk, A new modulated crystal structure of the ANS complex of the St Johns wort Hyp-1 protein with 36 protein molecules in the asymmetric unit of the supercell, 2020 Acta Cryst. D **76**, 653-667.

[91] J J Lovelace, V Petricek, G Murshudovc, G E O Borgstahl, Supercell refinement: a cautionary tale, 2019 Acta Cryst. D **75**, 852-860.

[92] J Porta, J J Lovelace, G E O Borgstahl, How to assign a (3 + 1)-dimensional superspace group to an incommensurately modulated biological macromolecular crystal, 2017 J. Appl. Cryst. **50**, 1200-1207.

[93] J J Lovelace, P D Simone, V Petricek, G E O Borgstahl, Simulation of modulated protein crystal structure and diffraction data in a supercell and in superspace, 2013 Acta Cryst. D **69**, 1062-1072.

[94] J Porta, J J Lovelace, A M M Schreurs, L M J Kroon-Batenburg, G E O Borgstahl, Processing incommensurately modulated protein diffraction data with Eval15, 2011 Acta Cryst. D **67**, 628-638.

[95] Hielscher, A. H., Tittel, F. K., Jacques, S. L. (1995). Imaging in biological tissues by means of diffraction tomography with photon density waves. Proceedings of SPIE - The International Society for Optical Engineering, 2326, 75-85. https://doi.org/10.1117/12.200865

[96] M D Wheelock, J P Culver, A T Eggebrecht, High-density diffuse optical tomography for imaging human brain function, Rev. Sci. Instrum. 90, 051101 (2019); doi: 10.1063/1.5086809

[97] M Rozycka, S Lenczowski, W Sawicki, W Baranska, K Ostrowski, Optical diffraction as a tool for semiautomatic, quantitative analysis of tissue speciments, 1982 Cytometry **2**, 244-248.

[98] M M Mareel, G K De Bruyne, K Ostrowski, M Rozycka, P Strojny, A Dziedzic-Goclawska, S Lenczowski, W Grzesik, J Kieler, Numerical evaluation of changes in the cytoplasmatic microtubule complex C3H mouse cells by optical diffractrometry and of changes in cell shape by Fourier analysis, 1986 Cytometry **7**, 18-24.

[99] Dal Negro L, J. Lawrence, J. Trevino, Engineering Aperiodic spiral order in Nanophotonics: Fundamentals and device applications. In P. Bettoti (Ed.), Nanodevices for Photonics and Electronics. Advances and Applications (Pan Stanford, USA, 2016). pp.57-125.

[100] M E Pollard, G J Parker, Low-contrast bandgaps of a planar parabolic spiral lattice, 2009 Opt. Lett. **34**, 2805-2807

[101] E Maciá, Exploiting aperiodic designs in nanophotonic devices, 2015 Rep. Prog. Phys. **75**, 036502.

[102] L Dal Negro, J. Lawrence, J. Trevino 2012, Analytical light scattering and orbital angular momentum spectra of arbitrary Vogel spirals, Opt. Express **20**, 18209.

[103] J Trevino, H Cao, L Dal Negro, Circularly symmetric light scattering from nanoplasmonic spirals, 2011 Nano Lett. **11**, 2008-2016.

[104] N Rivier, Crystallography of spiral lattices, 1988 Mod. Phys. Lett. B **2**, 963-960.

[105] N Rivier, A botanical quasicrystal, 1986 J. Phys. Colloques **47**, C3-299-C3-309.

[106] IUCr Online Dictionary of Cristallography. https://dictionary.iucr.org/Quasicrystal. Last accessed 4 March 2021.

[107] A H Boerdijk, Some remarks concerning close-packing of equal spheres, 1952 Philips Res. Rep. **7**, 303-13.

[108] H S M Coxeter, The simplicial helix and the equation $\tan n\theta = n \tan \theta$, 1985 Canad. Math. Bull. **28**, 385-393.

[109] J F Sadoc, N Rivier, Boerdijk-Coxeter helix and biological lattices as quasicrystals, 2000 Mat. Sci. Eng. A **294-296**, 397-400.

[110] J F Sadoc, N Rivier, Boerdijk-Coxeter helix and biological lattices, 1999 Eur. Phys. J. B , **12**, 309-318.

[111] D S Goodsell, Symmetry at the cellular mesoscale, 2019 Symmetry **11**, 1170.

[112] F H C Crick , J D Watson, The structure of small viruses, 1956 Nature (London) **177**, 473-5.

[113] D L D Caspar , Structure of tomato bushy stunt virus, 1956 Nature (London) **177** 475-7.

[114] A Klug, J T Finch, R E Franklin, The structure of turnip yellow mosaic virus: X-ray diffraction studies, 1957 Biochim. Biophys. Acta **25**, 242-252.

[115] DLD Caspar, Assembly and Stability of the Tobacco Mosaic Virus Particle, 1964 Advances in Protein Chemistry, **18**, 37-121.

[116] R E Franklin, Structure of Tobacco Mosaic Virus, 1955 Nature, **175**, 379 -381.

[117] R Franklin, D L D Caspar, A Klug, The structure of viruses as determined by X-ray diffraction, in *Plant Pathology: Problems and Progress 1908-1958*, Holton C S *et al.* (eds.) (Madison Univ. Wisconsin Press, 1959) 447-461.

[118] R Franklin, A Klug, The splitting of layer-lines in X-ray fibre diagrams of helical structures: Applications to tobacco mosaic virus, 1955 Acta Crystallog. **8**, 777-780.

[119] Note that this geometrical constraint does not operate in the case of helical viruses, which are open along the helical axis and can accommodate a nucleic acid of any length inside their capsids.

[120] H Naitow, J Tang, M Canady, R B Wickner, J E Johnson, L-A virus at 3.4 $\mathring{A}$ resolution reveals particle architecture and mRNA decapping mechanism, 2002 Nature Structural Biology, **9** 725-728.

[121] S J Flint, L W Enquist, V R Racaniello, A M Skalka, *Principles of virology, Molecular biology, Pathogenesis, and Control of Animal Viruses,* 2nd Ed. (ASM Press, Washington 2004).

[122] D L D Caspar, A Klug, Physical principles in the construction of regular viruses, 1962 Cold Spring Harbor Symp. Quant. Biol. **27** 1-24.

[123] M Goldberg, A class of multi-symmetric polyhedra, 1937 Tohoku Math. J. **43**, 104-108.

[124] H Takakura, C Pay-Gómez, A Yamamoto, M de Boissieu, A P Tsai, Atomic structure of the binary icosahedral Yb-Cd quasicrystal, Nature Materials **6** , 58 (2007).

[125] For $T \geq 7$ the capsid can appear in two different enantiomorphic forms, obtained by permuting the Goldberg indices $h \leftrightarrow k$, respectively. An example is shown in Fig.16 for the case $h = 2$, $k = 1$ (solid triangle) and $h = 1$, $k = 2$ (dashed triangle). The corresponding polyhedra are mirror images to each other, and are respectively labeled as $T = 7d$ (dextro form) and $T = 7l$ (levo form).

[126] I Rayment, T S Baker, D L D Caspar, W T Murakami, Polyoma virus capsid structure at 22.5 $\mathring{A}$ resolution, 1982 Nature (London) **295** , 110-115.

[127] R Twarock R, A tiling approach to virus capsid assembly explaining a structural puzzle in virology, 2004 J. Theor. Bio. **226** , 477-482.

[128] R Twarock, Mathematical virology: a novel approach to the structure and assembly of viruses, 2006 Phil. Trans. R. Soc. A **364**, 3357-3373.

[129] A Janner, Towards a classification of icosahedral viruses in terms of indexed polyhedra, 2006 Acta Cryst. A **62** , 319-330.

[130] A Janner, From an affine extended icosahedral group towards a toolkit for viral architecture, 2013 Acta Cryst. A**69**, 151-163.

[131] M Gardner, *Penrose Tiles to Trapdoor Ciphers... and the Return of Dr. Matrix*, (Cambridge University Press, Cambridge, 1997) p.24.

[132] P Natarajan, J E Johnson, Molecular packing in virus crystals: geometry, chemistry, and biology, 1998 J. Struct. Biol. **121**, 295-305.

[133] S C Harrison, Structure of tomato bushy stunt virus: Three-dimensional X-ray diffraction analysis at 30 Å resolution, 1971 Cold Spring Harbor Symp. Quant. Biol. **36** , 495-501.

[134] J W Erickson, E A Frankenberger, M G Rossmann, G S Shay Fout, K C Medappa, R R Rueckert, Crystallization of a common cold virus, human rhinovirus14: "isomorphism" with poliovirus crystals, 1983 Proc. Natl. Acad. Sci USA **80**, 931.

[135] T Lin, Z Chen, R Usha, C V Stauffacher, J B Dai, T Schmidt, J E Johnson, The refined crystal structure of Cowpea Mosaic Virus at 2.8 Å resolution, 1999 Virology **265**, 20-34.

[136] L Gan, J E Johnson, An optimal exposure strategy for cryoprotected virus crystals with lattice constants greater than 1000 Å, 2008 J. Synchrotron Rad. **15**, 223-226.

[137] I Rayment, Animal virus structure, in *Biological Macromolecules and Asemblies*, vol. **1** ed. McPherson (John Wiley & Sons 1984).

[138] P Schellenberger, G Demangeat, O Lemaire, C Ritzenthaler, M Bergdoll, V Oliéric, C Sauter, B Lorber, Strategies for the crystallization of viruses: using phase diagrams and gels to produce 3D crystals of Grapevine fanleaf virus, 2011 J. Struct. Biol. **174** , 344-351.

[139] E L Albuquerque, U L Fulco, E W S Caetano, V N Freire, *Quantum Chemistry Simulation of Biological Molecules* (Cambridge University Press, Cambridge, 2021) Chaps. 13-14.

[140] M F M Sciacca, C La Rosa, D Milardi, Amyloid-mediated mechanisms of membrane disruption, 2021 Biophysica **1**, 137-156.

[141] M Iafisco, J M Delgado-López, Biomimetic growth of calcium phosphate crystals, 2018 Crystals **8**, 5.

[142] M Vallet-Regí, A J Salinas, J Ramírez-Castellanos, J M González-Calbet, Nanostructure of Bioactive Sol-Gel Glasses and Organic-Inorganic Hybrids, 2005 Chem. Mater. **17**, 1874-1879.

[143] M Torres, G Pastor, I Jiménez, J. Fayos, Geometric models for continuous transitions from quasicrystals to crystals, 1989 Phil. Mag. Lett. **59**, 181-188.

[144] M Torres, G Pastor, I Jiménez, From the decagonal phase to a related crystalline ones, 1990

Phil. Mag. Lett. **61**, 319-325.

[145] A L Mackay, Generalized structural geometry, Acta Cryst. A 1974, **30** , 440-447.

[146] A L Mackay, Generalised crystallography, Comps. Math. Appls. 1986 **12B** , 21-37.

[147] A L Mackay, Generalised crystallography, J. Mol. Struct. (Theochem) 1995 **336** , 293-303.

[148] A L Mackay, Generalized crystallography, Struct. Chem. 2002 **13**, 215-220.

[149] H Bohr, *Collected Mathematical Works. II Almost periodic functions* (Copenhagen: Dansk Matematisk Forening, 1952).

[150] R Penrose, *The Road to Reality - A Complete Guide to the Laws of the Universe* (Jonathan Cape, London, 2004) Chap. 9.

TABLE I: Virus crystals crystallographic data including the triangulation number (T), the capsid diameter, the spatial group (SG), and the lattice parameters. Key: Black beetle virus (BBV), tomato bushy stunt virus (TBSV), cowpea mosaic virus (CPMV), flock house virus (FHV), southern bean mosaic virus (SBMV), HK97 bacteriophage, Nodamura virus (NOV), Coxsackie virus (CVB3), grapevine fanleaf virus (GFLV).

VIRUS	T	$\varnothing$ (nm)	SG	a, b, c (nm)	α, β, γ (°)	REF
BBV	3	33.2	$P4_232$	36.2	90.0	[132]
TBSV	3	34.6	$I23$	38.6	90.0	[133]
Polioma	$7d$	49.5	$I23$	57.2	90.0	[134][126]
CPMV	1	30.6	$P6_122$	45.1 45.1 103.8	90.0 90.0 120.0	[135]
FHV	3	33.4	$R3$	32.36	67.7	[132]
SBMV	3	30.2	$R32$	31.79	63.435	[132]
HK97	$7l$	60.0	$P4_32_12$	101.0 101.0 73.0	90.0 90.0 90.0	[136]
Poliovirus	1	32.0	$P2_12_12$	32.4 35.9 38.1	90.0 90.0 90.0	[137]
Rhinovirus	1	31.4	$P2_12_12$	32.3 35.8 38.0	90.0 90.0 90.0	[134]
NOV	3	34.8	$P2_1$	56.21 35.41 61.28	90.0 110.9 90.0	[132]
GFLV	1	30.6	$P1$	27.84 29.83 29.16	102.0 116.4 108.2	[138]